Numerical simulations of sink-flow boundary layers over rough surfaces

J. Yuan[1, a)] and U. Piomelli[1, b)]
Department of Mechanical and Materials Engineering, Queen's University, Kingston, Ontario, K7L 3N6, Canada

(Dated: 7 April 2015)

Turbulent sink flows over smooth or rough walls with sand-grain roughness are studied using large-eddy and direct numerical simulations. Mild and strong levels of acceleration are applied, yielding a wide range of Reynolds number ($Re_\theta = 372 - 2748$) and cases close to the reverse-transitional state. Flow acceleration and roughness are shown to exert opposite effects on boundary-layer integral parameters, on the Reynolds stresses, budgets of turbulent kinetic energy, and properties of turbulent structures in the vicinity of the rough surface; statistics exhibit similarity when plotted using inner scaling for cases with the same roughness Reynolds number, k^+. Acceleration leads to a decrease of k^+, while roughness increases it. For cases with higher k^+, the low-speed streaks become destabilized, and turbulent structures near the wall are distributed more uniformly in the wall-parallel plane; they are less extended in the streamwise direction, but more densely distributed. Higher k^+ also causes decorrelation of the outer-layer hairpin packets with the near-wall structures, probably due to the direct impact of random roughness elements on the hairpin legs. Wall-similarity applies for the fully turbulent cases, in which the outer-layer turbulent statistics are affected by acceleration only. It is shown that being in the hydraulically-smooth regime is a necessary condition for reverse-transition, supporting the idea that relaminarization starts from the inner region, where roughness effects dominate.

[a)] junlin.yuan@queensu.ca
[b)] ugo@appsci.queensu.ca

I. INTRODUCTION

Roughness plays an important role in many fields of study. A substantial amount of work has been carried out to understand the dynamics of turbulent flows over rough walls, both for engineering and atmospheric applications. Reviews by Raupach and co-workers[1,2] and Finnigan[3] summarize the research on roughness in atmospheric applications, while those by Raupach, Antonia, and Rajagopalan[2] and Jiménez[4] discuss engineering flows.

Most of the investigations of roughness effects on turbulence have concentrated on canonical flows: zero-pressure-gradient (ZPG) boundary layers, channels and pipes. Experimentally, several forms of roughness have been studied (sand-grain, rods, perforated plates, wire screens, protuberances) that span the transitional and the fully rough regimes. The increase in wall-normal fluctuations near the wall[5] and the decreased anisotropy of the Reynolds stresses[6] have been observed in many studies. Another issue that has received some attention is the height above which roughness effects do not propagate, which depends on the fluid-dynamical quantity examined but is of the order of $3 - 5k_s$[2,7,8] (where k_s is the equivalent sand-grain roughness height, defined as the mean height of the equivalent sand-grain roughness that produces the same amount of mean velocity deficit in the overlap region as the roughness in question). It is also important to observe that the roughness geometry plays a role: compared to three-dimensional roughness (*e.g.*, meshes, sand-grains), two-dimensional roughness (*e.g.*, spanwise rods and bars) leads to significant changes in the outer flow, different energy production and turbulence diffusion, and larger scales of the outer-layer structures, even when the same roughness function is produced.[9,10] Additionally, recent studies on realistic roughness show that the surface topographical features affect the strong energy-producing turbulence events near the wall, and thus affect friction and heat transfer.[11–13] In the current study, the "outer layer" in a flow over roughness refers to the region outside the roughness sublayer.

The main obstacle to simulate directly rough-wall flows is the computational cost (see the discussion in Jiménez[4]): to achieve fully rough flows one needs $k^+ > 80$ (where k is the roughness height, and a $+$ indicates quantities normalized by the friction velocity and viscosity); at the same time one needs to have a domain large enough to minimize contamination of the entire boundary layer by the roughness, as well as blockage effects ($\delta > 20k$, where δ is the boundary layer thickness). Meeting both criteria is expensive, and numerical simulations that have been performed so far relax one or both of these requirements. Direct numerical simulations (DNS) focusing on transitionally rough flows include those carried out by Orlandi and Leonardi[14], Bhaganagar and co-workers[15–17], Scotti[18], and Lee and co-workers[19,20]; fully rough flows are reached with higher blockage ratio in the DNS studies by Leonardi *et al.*[21], and Ikeda and Durbin[22], for instance. Many of the simulations described above use Immersed-Boundary Methods (IBMs) to represent the obstacle, *i.e.*, use localized forces to simulate complex geometries within a simple (usually Cartesian) grid structure.

Turbulent boundary layers subject to a favorable pressure gradient (FPG) are found in many engineering applications, including airfoils, turbine blades or curved ducts; in many of these applications roughness is also important. A vast body of literature on smooth-wall FPG boundary layers exists. The review by Narasimha and Sreenivasan[23] remains a landmark, and outlines many of the open questions and issues. Here, we only summarize the principal ones. It is known that, when the acceleration is sufficiently large, the flow may revert to a quasi-laminar state; the state between fully turbulent flow and fully relaminarized flow is

called "reverse-transitional". The acceleration can be characterized by the parameter $K = (\nu/U_\infty^2)(dU_\infty/dx)$ (U_∞ is the freestream velocity). In sink flows (in which the acceleration acts for an infinite distance and K is not a function of the streamwise location, i.e., the accelerating flow is equilibrium), Spalart [24] showed that turbulence cannot be sustained if K is higher than a critical value, K_{crit}, between 2.5×10^{-6} to 3.0×10^{-6}. In realistic spatially developing boundary layers, of course, the acceleration cannot act for infinite distances, and complete relaminarization occurs rarely. However, the state of the flow is still significantly altered by strong acceleration, and even the mean velocity profile is modified. Reviews of current knowledge can be found in several articles[23,25,26] and in more recent studies[27–29]. Experimental investigations of relaminarization due to flow acceleration started in the early 1960s. Among the major findings of these studies was the fact that, at least in the outer region of the boundary layer, dissipation remains smaller than production. Narasimha and Sreenivasan [25] conjectured that, since the streamwise and wall-normal fluctuations do not lose their correlation, relaminarization is due to pressure forces dominating over nearly frozen Reynolds stresses. Recent simulations of accelerating flows over smooth, flat plates[28–30] show that, in the region of maximum acceleration, frozen turbulence advected from upstream is still present, but does not keep up with the freestream acceleration.

The sink flow is the simplest accelerating boundary layer and has been studied numerically[24] and experimentally[31–34]; in this type of flows, K and the Reynolds number remain constant, resulting in statistical similarity in the flow direction. Therefore, a sink flow is substantially less expensive computationally, compared to spatially developing accelerating flows. In smooth-wall sink flows, typical responses of the turbulence include thickening of the viscous sublayer, damping of fluctuations especially in the wall-normal component, lower bursting rate, and larger near-wall coherent structures.

More recent studies have investigated the interaction between roughness and pressure gradients. Tachie *et al.*[35] conducted experiments in flows over bar roughness under FPG due to converging side-walls in an open channel. From the study of a wide range of k_s^+ they concluded that, while in the hydraulically smooth regime the flow responses were similar to those on a smooth wall, in the cases of fully rough flows no apparent FPG effect was observed on drag characteristics, on the mean flow, or on turbulent quantities. However it remained unclear whether this conclusion applied also to cases with FPG generated by converging top walls. Tachie and Shah[36] studied the same type of roughness with an inclined bottom wall, using stronger acceleration. It was found that near-wall flows were still governed by roughness effects, while, in the outer layer, acceleration decreased Reynolds stresses and increased the triple velocity correlations and transport of turbulent kinetic energy. Both these studies featured strongly non-equilibrium accelerating flows.

Cal *et al.*[37,38] studied quasi-equilibrium boundary layer flows on a tilted plane with sand-grain roughness and mild acceleration; the acceleration was applied for a considerable distance for both the fully rough and transitionally rough flows. They observed a general increase of friction coefficient C_f and decrease of Reynolds number based on momentum thickness, Re_θ, as acceleration was imposed on the rough wall. Competing effects of K and roughness were found on the mean flow, and on the Reynolds stresses in the outer layer; close to the wall, however, acceleration significantly intensified the fluctuations, an effect opposite to a smooth-wall flow. It is not clear whether these effects were due to the fact that the flow is spatially developing, or to the mild levels of acceleration used.

The interaction between strong acceleration and near-wall roughness effects was observed

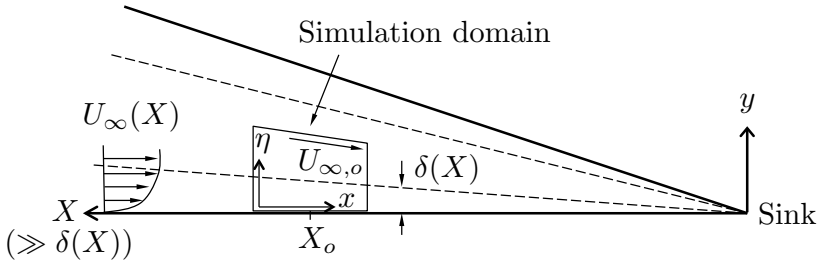

FIG. 1. Schematic of the simulation domain in a sink flow. From here on η is written as y for simplicity.

by Piomelli and Yuan[28] in large-eddy simulations of strongly non-equilibrium boundary layer flows: under strong freestream acceleration, relaminarization was achieved over both the smooth wall and a rough surfaces with low roughness height. However, when the roughness was significant, the accelerating flow did not relaminize; instead, the generation and growth of streaks were disrupted, and the near-wall wall-normal and spanwise fluctuations did not decrease during acceleration. It was concluded that the inner layer plays a dominant role in the relaminarization process.

To further understand the interaction of strong FPG and roughness, it appears desirable to remove the effects of spatial development and investigate the simplest equilibrium accelerating flow, the sink flow. It is the objective of this paper to carry out a parametric study of both roughness and acceleration in the transitionally rough regime, with a wide range of K. The combination of acceleration and roughness leads mostly to fully turbulent flows, with another two cases close to the reverse-transitional state. We focus on the fully turbulent flows to investigate the combined effects on turbulent statistics and coherent structures. In the following, first we present the model used, including the numerical scheme, the turbulence parameterization and the modelling of the roughness. We will then show the validation of the model, and discuss the simulation results.

II. PROBLEM FORMULATION

The incompressible sink-flow of a Newtonian fluid is governed by the equations of conservation of mass and momentum:

$$\frac{\partial u_i}{\partial x_i} = 0, \tag{1}$$

$$\frac{\partial u_j}{\partial t} + \frac{\partial u_i u_j}{\partial x_i} = -\frac{\partial P}{\partial x_j} + \frac{1}{Re}\nabla^2 u_j + G_j + F_j. \tag{2}$$

The equations have been made dimensionless using a reference velocity and length, U_∞ and X (which will be specified later). x_1, x_2 and x_3 (or x, y and z) are, respectively, the streamwise, wall-normal and spanwise directions, and u_j (or u, v and w) are the velocity components in those directions; $P = p/\rho$ is the modified pressure, ρ the density and $Re = U_\infty X/\nu$ the Reynolds number. The term F_j in Eq. (2) is a body force imposed by the immersed boundary method used to impose non-slip boundary conditions on the rough surface, and will be explained later.

The mathematical treatment of the sink flow follows the approach proposed by Spalart:[24] the domain is transformed into similarity coordinates (x, η, z), with $\eta = yX_o/X$. The schematic of a sink flow on the (x, η)-plane is shown in Fig. 1. Here, X_o is a constant related to the mean flow-rate towards the sink, and X the distance from the sink. If the boundary-layer thickness δ is much smaller than X, we can consider a domain centered around the position X_o, and assume that the turbulence is spatially homogeneous since the statistical quantities vary with $X \gg \delta$, and the turbulent fluctuations varie slowly compared with δ. The reference velocity and the reference length for the streamwise locations inside the domain can then be approximated by $U_{\infty,o}$ (the free-stream velocity at $x = X_o$) and X_o. Note that both reference quantities are independent of K; in fact, K is the normalized viscosity, $K = \nu/Q$, where $Q = U_\infty(X)X = U_{\infty,o}X_o$ is a constant; thus K is determined by ν alone. The effect of the acceleration is then included through growth terms that can be obtained from the transformation of the equations into the similarity coordinates, followed by a multiple-scale procedure to simplify the equations. The growth terms are given by[24]

$$G_1 = -\frac{\langle u \rangle}{X_o}(\langle u \rangle + 2u') + \frac{U_\infty^2}{X_o}, \qquad G_2 = 0, \qquad G_3 = -\frac{\langle u \rangle}{X_o}w', \tag{3}$$

where $\langle \cdot \rangle$ denotes an appropriate average (in this case, carried out over time and the homogeneous flow directions), and u' and w' are fluctuations from the averages. With this transformation, only two parameters are present: the acceleration parameter K and the roughness height, $\overline{k} = k/X_o$. For simplicity, η is replaced with y in the following.

In large-eddy simulations (LES), Eqs. (1) and (2) are solved for filtered quantities, and the divergence of the sub-grid stress tensor, $\tau_{ij} = \overline{u_i u_j} - \overline{u}_i \overline{u}_j$, appears on the right-hand-side of the momentum equation. In the present study, τ_{ij} is modeled using the Lagrangian Dynamic Eddy-Viscosity model[39], due to its capability of capturing flow heterogeneity by tracking the fluid particle-paths in time.

The simulations are performed using a well-validated code that solves the governing equations (1) and (2) on a staggered grid using second-order, central differences for all terms, a second-order accurate semi-implicit time advancement, and MPI parallelization[40]. Periodic boundary conditions are used in the streamwise and spanwise directions (since the flow is assumed to be homogeneous on the scale $\delta \ll X$). A free-slip boundary condition is imposed on the top boundary.

On the bottom wall, an immersed boundary method based on volume-of-fluid method is used to impose the non-slip conditions on the roughness surface. We use the roughness model proposed by Scotti[18]: a virtual sand-paper is constructed from randomly oriented and distributed ellipsoids of the same shape and size (with the three semi-axes equaling k, $1.5k$, and $2k$); this model was found to give $k_s = k$ in the transitionally rough regime. The volume fraction of each grid cell occupied by the fluid (volume-of-fluid, or ϕ) is calculated in pre-processing. Visualization of the surface with $\phi = 0.5$ (representative of the shape of the rough wall) is shown in Fig. 2. The implementation of the immersed boundary method is detailed in Appendix A.

A total of 12 simulations were run, identified by KnRm, where $n = 1, ..., 4$ denotes varying acceleration parameters K, and $m = 0, ..., 3$ different roughness heights. Table I gives the values of K, $\overline{k}$, and k^+ in all cases. k^+ values within a 25% range are considered constant; thus, we will consider cases K2R1, K3R2 and K4R3 as having approximately the same value of k^+. In all cases, $\delta/k \geq 25$, and k^+ is in the transitionally rough regime; Re_θ ranges

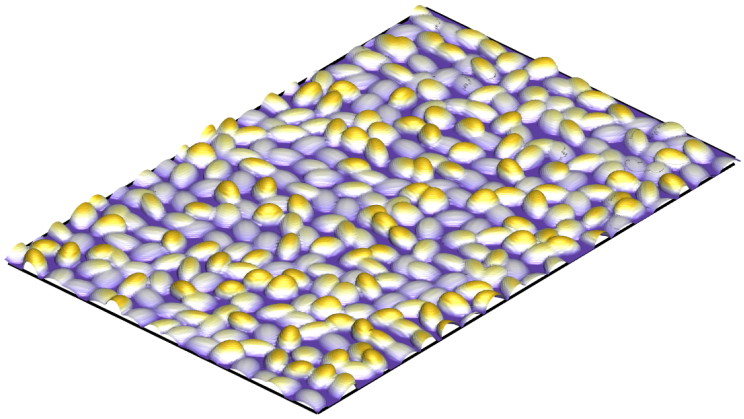

FIG. 2. Visualization of sand-grain roughness R3 for 1/8 of the domain using the iso-surface of ϕ with value 0.5 (i.e., borders of roughness).

TABLE I. Summary of simulation parameters. Values of roughness Reynolds number k^+.

	K1	K2	K3	K4
K	0.45×10^{-6}	0.80×10^{-6}	1.50×10^{-6}	2.50×10^{-6}
Grid[a]	768×245×512	768×245×512	768×245×512	384×245×256
R0 (smooth)	0	0	0	0
R1 ($\overline{k} = 3.0 \times 10^{-4}$)	36.3	20.2	10.6	–
R2 ($\overline{k} = 6.0 \times 10^{-4}$)	–	45.9	23.4	13.4
R3 ($\overline{k} = 9.5 \times 10^{-4}$)	–	–	41.6	23.8

[a] The number of grid in y-direction varies between 218 and 273 for resolving roughness with various heights; the value listed is the mean.

between 372 and 2853. As will be shown later, only cases K4R0 and K4R2 are close to the reverse-transitional state.

Due to the wide range of Reynolds numbers, LES must be used for the cases with milder accelerations (K1 and K2), while direct simulations are used for cases K3 and K4. The domain size in all cases is $0.2X_o \times 0.06X_o \times 0.04X_o$, equivalent to approximately $9\delta \times 3\delta \times 2\delta$. The domain sizes in x and z directions are similar to those used by Spalart[24], and the streamwise and spanwise two-point correlations of the streamwise turbulent fluctuations, calculated at $y \leq 0.5\delta$, fall below 0.1 at half the domain length or width.

Uniform grids are used in x and z directions, while stretching is applied in the y direction outside of the roughness layer. In DNS, Δx^+ and Δz^+ are less than 15 and 4, respectively, and $\Delta y^+ < 0.5$ in the region below the top of the roughness elements ($y \lesssim 1.5k$). In LES, $\Delta x^+ = 17 - 30$, $\Delta z^+ = 6 - 9$, and $\Delta y^+ < 1$ in the region $y \lesssim 1.5k$. The stretching rate of the y grid is less than 4% in all cases. Note that even the LES is highly resolved, with grid sizes only marginally worse than those of direct simulations of smooth-wall flows in the literature. Between 20 and 100 million total grid points were required. The roughness geometry is resolved by at least 16 grid points in the (x, z) plane, and by more than 30 grid points in the y direction; this surface resolution is similar to the one used in the work of

Scotti[18], where the current roughness model was validated. The simulations were initialized by a calculation at a lower value of K, and integrated in time for $15\delta/u_\tau$ units to achieve a statistically steady state. Data was then collected for 30 additional time units to calculate statistics.

In the following, the angle brackets $\langle\cdot\rangle$ denote quantities that are averaged in time and over the homogeneous directions x and z. $U_i(y)$ is the time- and space-averaged velocity

$$U_i(y) = \langle u_i(x,y,z,t)\rangle, \tag{4}$$

whereas $\langle\cdot\rangle_{xz}$ and $\langle\cdot\rangle_t$ denote averaging over the homogeneous directions or time.

$$\widetilde{U}_i(x,y,z) = \langle u_i(x,y,z,t)\rangle_t - U_i(y) \tag{5}$$

is the deviation of the local time-averaged velocity from the time-and space-averaged one. Note that $\widetilde{U}_i(x,y,z)$ is non-zero only in the vicinity of the roughness. Turbulent fluctuations u_i' are calculated by subtracting the time-averaged velocity from the total one:

$$u_i'(x,y,z,t) = u_i(x,y,z,t) - \langle u_i(x,y,z,t)\rangle_t \tag{6}$$

$$= u_i(x,y,z,t) - \Big(U_i(y) + \widetilde{U}_i(x,y,z)\Big). \tag{7}$$

First and second moments of the velocity calculated using half the sample differed from those calculated using the full sample by less than 4%.

III. RESULTS

In this section, first the smooth-wall sink flows are compared with previous results. Then, the flow statistics (Sec. III B) are studied to investigate the start of reverse-transition in the context of rough-wall sink flows. Next, we focus on the fully-turbulent cases to determine what causes the gradual change to the reverse-transition state, and what the effects are on the statistics. To explain the flow statistics, the mean-flow structures (Sec. III C) and turbulent structures in both near-wall region (Sec. III D) and the outer region (Sec. III E) are then studied among the fully-turbulent cases.

A. Smooth-wall sink flow

The mean velocity and turbulent fluctuations of the highest- and lowest-K cases for smooth walls are compared in Fig. 3 with experimental[32,34] and other DNS results[24]. As K increases, U falls above the universal logarithmic law, and the slope slightly decreases from $1/\kappa$. Meanwhile, the inner peak of the streamwise Reynolds stress $\langle u'^2\rangle$ moves away from the wall due to the thickening of the viscous sublayer, and the wall-normal component $\langle v'^2\rangle$ is significantly reduced throughout the boundary layer. Good agreement is achieved with experimental results. Compared to DNS results obtained by Spalart[24], the current simulation gives a 4% lower friction velocity, shown by the higher maximum U^+, which is closer to the experimental results, as well as 8% lower peak for $\langle u'^2\rangle^+$. This is probably due to the finer grid size in the (x,z)-plane in wall units (at least twice finer than the former DNS) used in the current study; a grid-refinement study has shown that a finer grid leads to lower friction velocity, higher peak of $\langle u'^2\rangle^+$ and low peak of $\langle v'^2\rangle^+$.

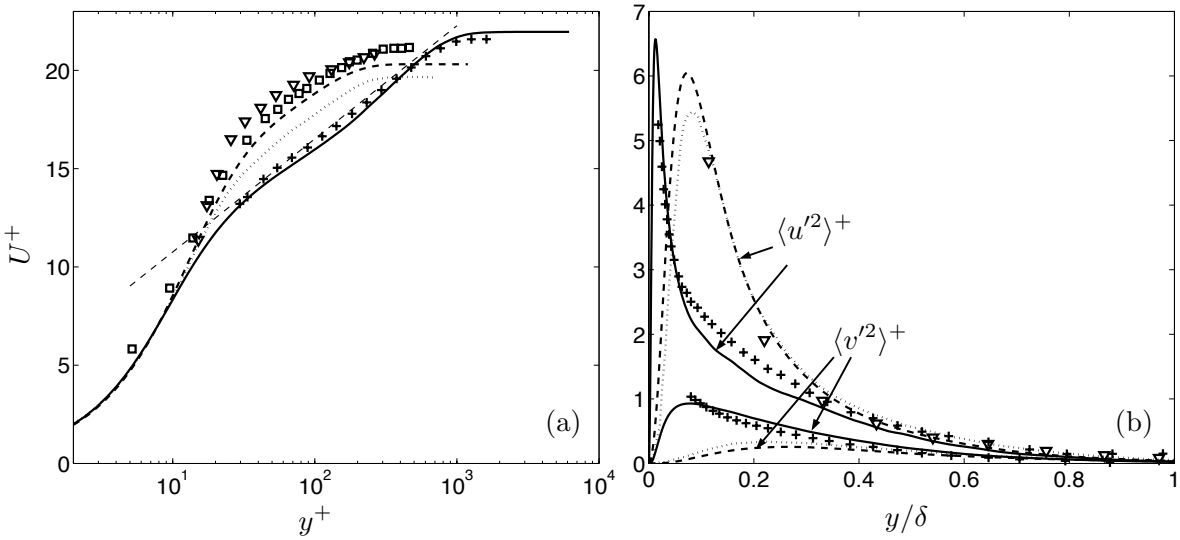

FIG. 3. Smooth wall simulations: —— $K = 0.45 \times 10^{-6}$, - - - $K = 2.5 \times 10^{-6}$. (a) Mean velocity; thin black dashed line: $U^+ = 1/0.41 \log y^+ + 5$; (b) Reynolds stresses. ····· Spalart DNS[24], $K = 2.5 \times 10^{-6}$; □ Dixit and Ramesh[34], $K = 2.18 \times 10^{-6}$; ▽ Jones and Launder[31], $K = 2.5 \times 10^{-6}$; + Jones *et al.*[32], $K = 0.54 \times 10^{-6}$. Superscript "+" indicates normalization in wall units.

The total shear stress and Reynolds shear stress for case K3R0 are compared with DNS and experimental results in Fig. 4. Excellent agreement is obtained, indicating that, despite the difference in friction velocity, the current results capture the same overall acceleration effects as the DNS.

The grid requirements for smooth-wall cases are assumed to apply to rough cases also, since, in the transitionally rough regime, the roughness scales are of the same order of the scales of near-wall structures. Additionally, the domain size of the smooth cases is deemed sufficient for the rough cases, assuming that roughness does not increase the scale of the largest eddies, which occur far from the wall, where the roughness is not expected to play a significant role; this assumption is supported by results from various authors, *e.g.*, Volino et al.[41] and Wu and Christensen[42], and will be validated *a posteriori* by examining the outer-layer structure size.

B. Flow statistics

Results of the boundary layer parameters are shown in Table II. The Reynolds number based on momentum thickness, Re_θ, and the friction coefficient

$$C_f = 2\left(\frac{u_\tau}{U_\infty}\right)^2, \tag{8}$$

where

$$u_\tau = \sqrt{-\langle f_d \rangle / \rho}, \tag{9}$$

are shown in Fig. 5. f_d is the sum of pressure and viscous drag on rough surfaces; its calculation is described in Appendix C. Good agreement is obtained with available experimental[31,34]

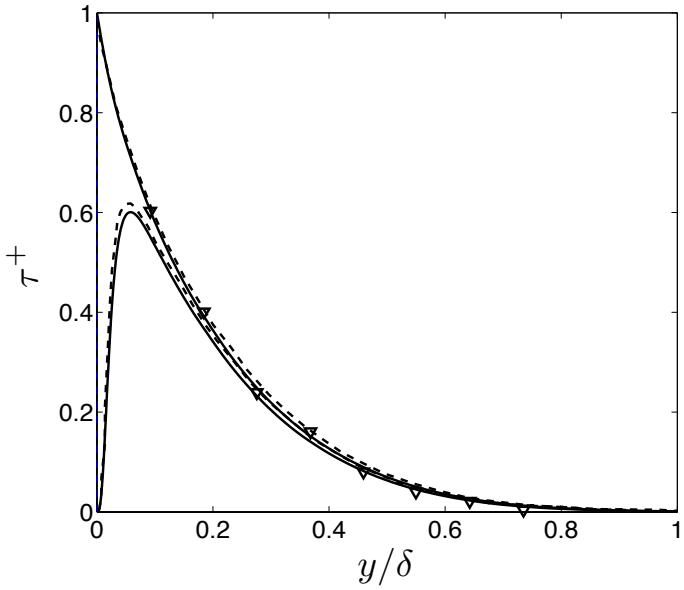

FIG. 4. Total shear stress and Reynolds shear stress in the smooth case with $K = 1.5 \times 10^{-6}$. —— current results; --- Spalart DNS[24]; ▽ Jones and Launder[31].

TABLE II. Boundary layer parameters in all cases. H is the shape factor; θ is the momentum thickness.

Case	k/δ (%)	Re_θ	$C_f \times 10^3$	H	$\delta^+_{99.9}$	$\overline{\delta}_{99.9}$	$\overline{\theta} \times 10^4$
K1R0	0	2037	4.15	1.32	1752	0.017	9.2
K1R1	1.9	2748	5.93	1.37	1874	0.015	12.7
K2R0	0	1248	4.48	1.35	1116	0.019	10.0
K2R1	1.7	1510	5.83	1.34	1166	0.017	12.1
K2R2	3.1	2028	7.49	1.34	1472	0.019	16.2
K3R0	0	662	4.88	1.43	584	0.018	9.9
K3R1	1.5	749	5.64	1.36	687	0.019	11.0
K3R2	2.9	1016	6.87	1.33	808	0.020	15.2
K3R3	4	1266	8.62	1.31	1028	0.024	19.1
K4R0	0	372	4.84	1.58	337	0.017	9.3
K4R2	2.9	484	6.19	1.39	462	0.021	12.1
K4R3	4.2	696	7.87	1.31	574	0.023	17.4

and numerical[24] smooth-wall data. Re_θ decreases with K and increases with roughness, as observed by Cal *et al.*[37]. C_f was found to increase with K by Cal *et al.*[37], while results obtained by Tachie *et al.*[35] showed negligible variation of C_f with K. In the current study, however, an increase of K with a constant $\overline{k}$ decreases C_f, while roughness increases C_f, as was observed in all studies. Notice that $u_\tau/U_\infty = (C_f/2)^{1/2}$ is only mildly affected by K [Fig. 5(c)]; also, the viscous length scale is

$$\overline{\delta_\nu} \equiv (\nu/u_\tau)/X_o = K(U_\infty/u_\tau). \tag{10}$$

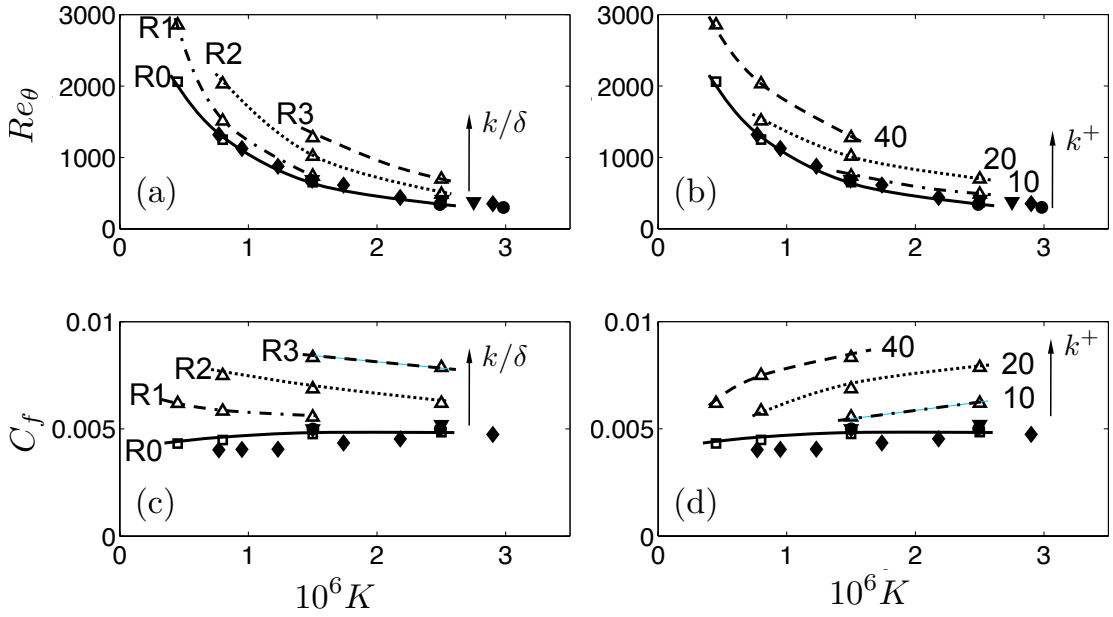

FIG. 5. Effects of roughness and acceleration on (a), (b) the Reynolds number and (c), (d) the friction coefficient. Lines connect cases with constant k/δ in (a) and (c), and cases with constant k^+ in (b) and (d). Hollow symbols are data from current study: □ smooth; △ rough. Solid symbols are reference data: ♦ Dixit and Ramesh[34]; • Jones and Launder[31]; ▼ Spalart[24].

Then, k^+, which can be written as

$$k^+ = \overline{k}/\overline{\delta_\nu} = \frac{(k/X_o)(u_\tau/U_\infty)}{K}, \tag{11}$$

can be viewed as a relative measure of the effects of roughness and acceleration, since the numerator is essentially determined by $\overline{k}$. Following the constant-k^+ lines in Fig. 5(b) and (d), it is found that, as K increases, Re_θ decreases, dominated by the acceleration effect, and C_f increases, dominated by the roughness effect.

Figure 6 shows the mean velocity profiles in wall units for calculations with increasing acceleration [Fig. 6(a)] and roughness height [Fig. 6(b)]. The zero-plane displacement, d is defined as the wall-normal location where the drag appears to act (*i.e.*, the centroid of the local drag profile). With the sand-grain model, d/k is around 0.8, insensitive to FPG (see Appendix A); this value is the same as that obtained by Scotti[18] in open-channel flow simulations, probably because the shape of the forcing distribution depends more on the type of roughness, compared to the effects of external conditions such as flow acceleration. Note that the various thicknesses are measured from the plane $y = d$.

In most cases (the main exception being the high-acceleration, low-roughness case, K4R2), we observe clearly a logarithmic layer, which acceleration displaces upwards and roughness downwards. Non-universal log-law constants have been used to describe equilibrium sink flows with similar or lower levels of acceleration compared to the current study[34,43], but in our calculations the von Kàrmàn constant κ (calculated by considering the plateau region of $y^+ dU^+/dy^+$) was found to be within the accepted range around the universal value ($\kappa \simeq 0.4$) except in case K4R2. In this case, $k^+ \simeq 10$, close to the hydraulically smooth regime, and the

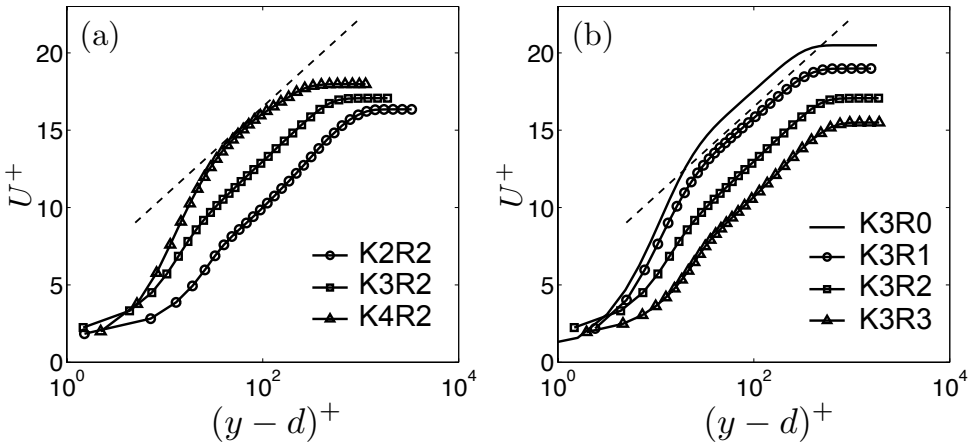

FIG. 6. Mean velocity profiles in inner scaling. (a) Effect of K; (b) Effect of $\overline{k}$. --- Universal logarithmic law.

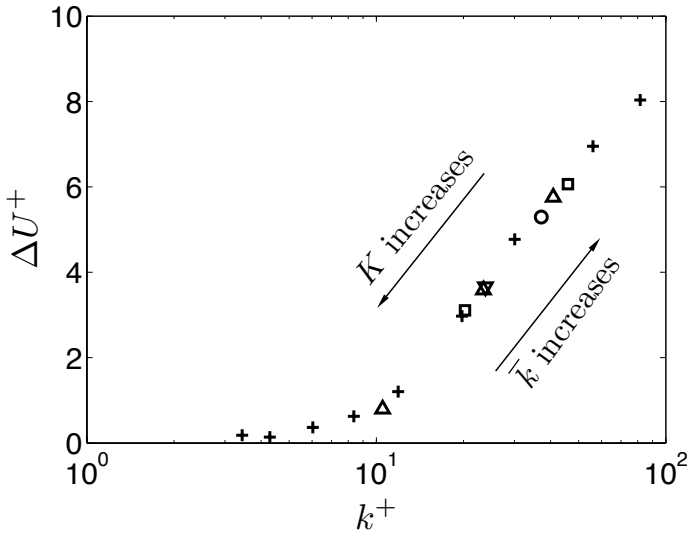

FIG. 7. Dependence of roughness function ΔU^+ (case K4R2 not shown) on k^+. Rough cases: ◯ K1, □ K2, △ K3, ▽ K4; + Colebrook[44].

pressure gradient is strong, leading to a case close to reverse transition. On the smooth wall, Dixit and Ramesh[43] observed a gradual 18% increase of κ as K increases from 7.7×10^{-7} to 2.9×10^{-6}; on the current R2 rough wall, the relatively sudden increase of κ as K approaches K4 indicates that flow reversion occurs only when the flow is nearly in the hydraulically smooth regime, where κ approaches the smooth-wall value; for higher k^+, κ is insensitive to the strengthening of acceleration.

Since the slope of the logarithmic region is close to the universal value, the roughness function can be defined as the offset of the logarithmic profile from the universal logarithmic law,

$$\Delta U^+ \equiv U^+ - \frac{1}{\kappa}\log(y-d)^+ - B, \tag{12}$$

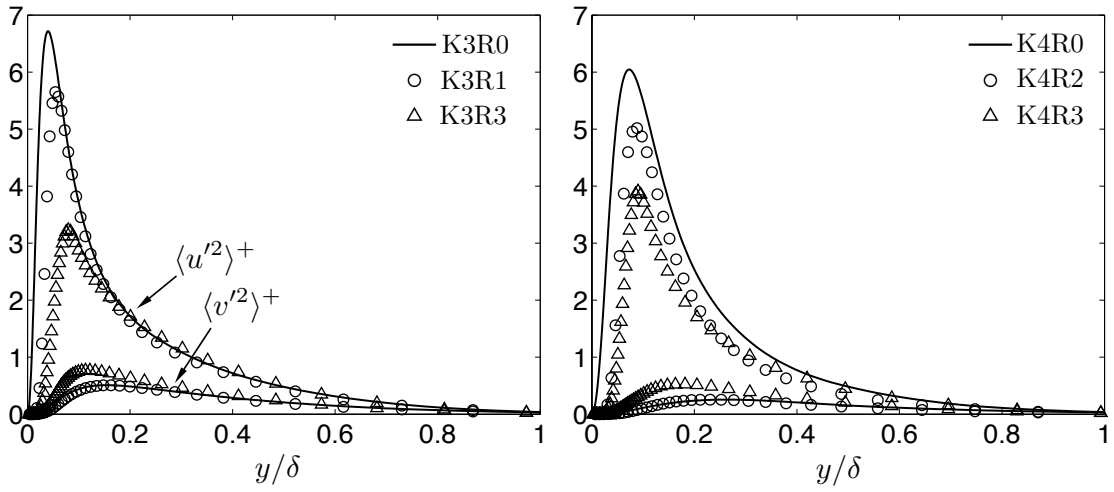

FIG. 8. Roughness effects on the streamwise and wall-normal components of the Reynolds stress tensor, normalized by u_τ, in cases with (a) K3 and (b) K4.

where $\kappa = 0.41$ and $B = 5.0$. From Fig. 7, we observe that the sink-flow results collapse with those from experimental studies on equilibrium pipe flows. The robustness of the dependence of the roughness function on the roughness Reynolds number may deserve further attention.

The roughness-induced momentum deficit is not dominantly affected by acceleration nor roughness; instead, it is affected by the ratio between the strengths of the two. In non-equilibrium accelerating boundary layers, Tachie *et al.*[35] found, based on the assumption of a universal log-law, that ΔU^+ is affected by roughness height but not by acceleration. This does not necessarily contradict the current results, since, in their studies, k^+ is not significantly affected by K either. The current work serves to clarify that both K and $\overline{k}$ are important in determining the mean velocity deficit in developed FPG flows.

The roughness effects on the Reynolds stresses are presented in Fig. 8, compared to the smooth case with the same K. It is known that, for low blockage ratio k/δ, three-dimensional roughness does not affect outer-layer Reynolds stresses in a high-Reynolds-number ZPG boundary layer, when normalized with u_τ. Here, it is found that wall similarity also applies to boundary layers that are subject to certain strength of acceleration, as shown by the K3 cases [Fig. 8(a)] and cases with weaker K (not shown); among the K3 cases, $Re_\theta = 625-1276$ and $k/\delta \leq 0.04$. The thickness of the roughness sublayer, defined as the layer where the statistics of the rough cases differ from the smooth one, is around $5k$, consistent with earlier observations of $3-5k_s$ for a variety of three-dimensional roughness. On the other hand, in the K4 cases [Fig. 8(b)] the Reynolds stresses do not collapse; specifically, the increase of $\langle u'^2\rangle$ due to roughness is less fast than that of u_τ^2, while the increase of $\langle v'^2\rangle$ is faster. In these cases, k/δ are similar to those in the K3 cases, but the Reynolds numbers are much lower ($Re_\theta = 372-696$). Case K4R0 and K4R2 are in the reverse-transitional state; a deviation is, therefore, expected from the outer-layer similarity hypothesis based on fully turbulent flows.

In Fig. 9, the Reynolds stresses are compared among three cases: cases K1R1 and K3R1 show the effects of K increase only, while cases K3R1 and K3R3 show the effects of $\overline{k}$ increase only. K1R1 and K3R3 have the same k^+ (≈ 40) while K3R1 corresponds to a lower k^+ (≈ 10). Similar to the effects on smooth-wall flows, an increase of K increases the streamwise component of the Reynolds normal stress in the near-wall region, and damps

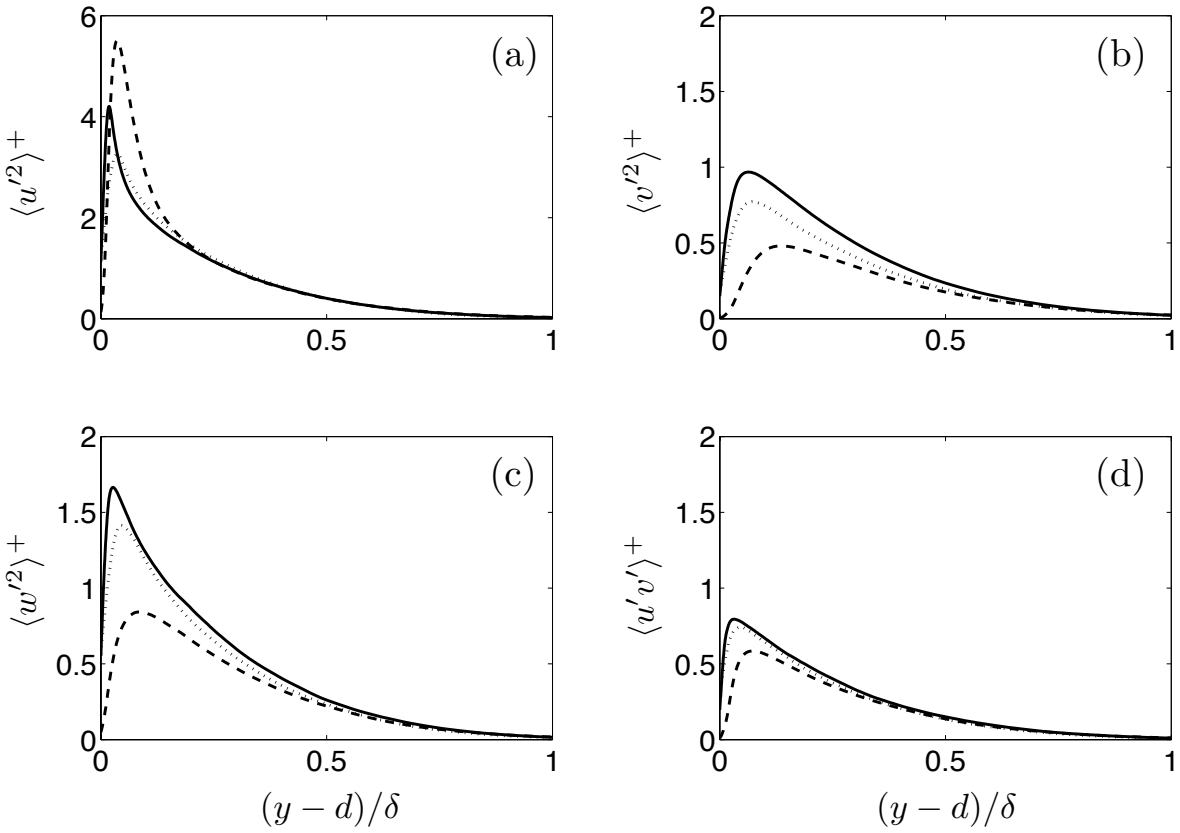

FIG. 9. Separate effects of K and $\overline{k}$ on the normal Reynolds stresses and the Reynolds shear stress. —— K1R1, - - - , K3R1, ····· K3R3.

the wall-normal and spanwise components; the Reynolds shear stress also decreases near the wall. On the other hand, an increase of $\overline{k}$ decreases the streamwise component and increases both the other two normal components of Reynolds stresses, and results in a higher $\langle u'v'\rangle^+$. The effects of K are visible throughout the lower half of the boundary layer (especially for v'^+ and w'^+), consistent with the observations by Cal *et al.*[38] that the u_τ scaling does not absorb the FPG effects. However, the current K effects appear to start from the inner peak, while in their studies, the K effects are significant throughout the boundary layer and appear to start from the outer layer. The roughness effect on $\langle u'^2\rangle^+$ in the current study is consistent with their observations, showing a significant decrease within the region $y-d<0.2\delta$, whereas its effects in $\langle v'^2\rangle^+$, $\langle w'^2\rangle^+$ and Reynolds shear stress are much more significant than in their studies, in which they were found to be minimal. Comparison between cases K1R1 and K3R3 shows that cases with the same k^+ give nearly identical Reynolds-stress profiles; the only difference is the slightly lower peak values in the case with higher K and higher $\overline{k}$.

The Reynolds stress anisotropy tensor b_{ij} is defined as

$$b_{ij}=\frac{\langle u_iu_j\rangle}{\langle u_ku_k\rangle}-\frac{\delta_{ij}}{3}. \tag{13}$$

Anisotropies for the same three rough cases are shown in Fig. 10. The outer-layer anisotropy (in the region $(y-d)>0.3\delta$) is dominantly determined by K, as shown by the collapse of

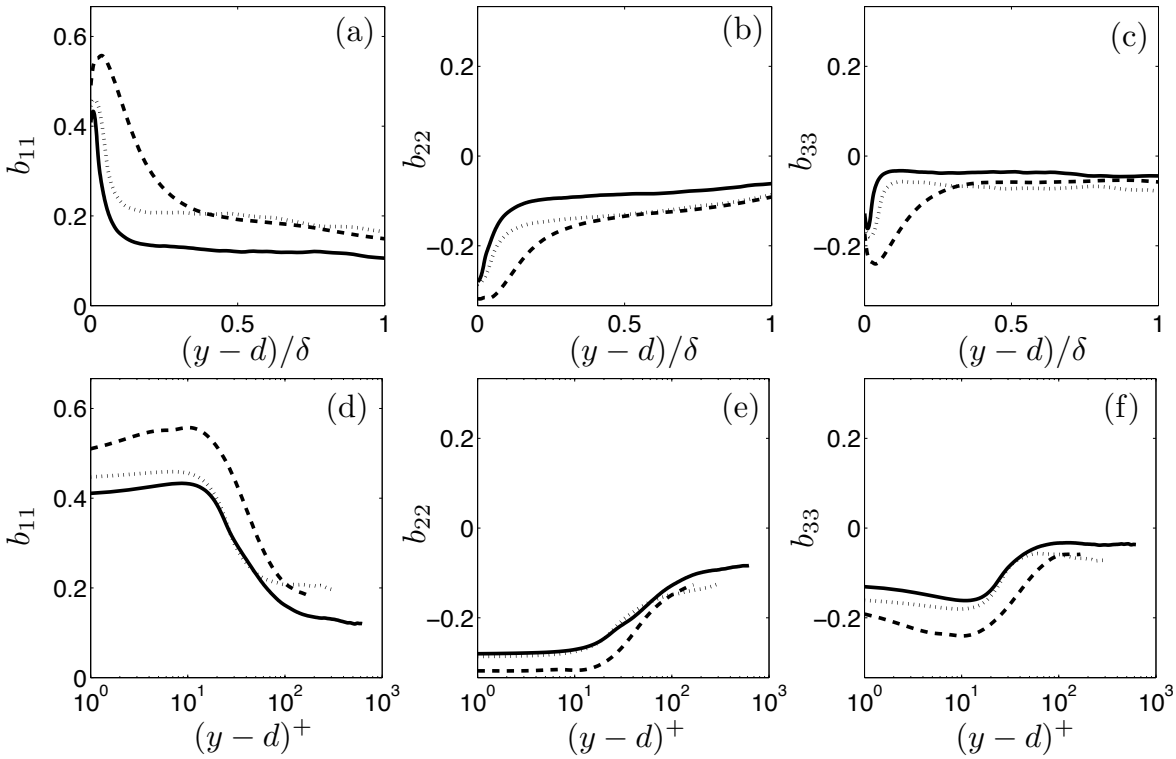

FIG. 10. Normal components of the anisotropy tensor for rough cases K1R1 (——), K3R1 (- - -), and K3R3 (····) plotted in (a)–(c) outer scaling and (d)–(f) inner scaling.

cases K3R1 and K3R3 in this region in Fig. 10 (a)–(c); this is consistent with the outer-layer similarity valid for cases outside of the reverse-transitional state. In the wall region, the anisotropy profiles mostly collapse for cases with $k^+ \approx 40$, as shown by cases K1R1 and K3R3 in the region $(y-d)^+ < 50$ in Fig. 10 (d)–(f), suggesting a near-wall similarity based on the roughness Reynolds number.

The near-wall turbulent-kinetic-energy (TKE) budgets are compared in Fig. 11, normalized by u_τ and δ_ν. Note that the effects of the growth terms have been included into energy production and mean-flow advection; the mean-flow advection is negligible for all three cases and thus is not presented. Cases K1R1 and K3R3 collapse well for all budget terms. The case with lower k^+, however, shows a peak of production closer to the wall, at $(y-d)^+ \approx 10$; the energy generated at this vertical location is transported towards the wall through viscous and turbulent diffusion (Fig. 11 (b) and (c)), and dissipated in the region $(y-d)^+ \lesssim 10$, where the viscous dissipation exhibits a peak (Fig. 11 (a)). The higher-k^+ cases show much weaker energy diffusion, especially viscous, due to the fact that these cases are much farther away from the hydraulically-smooth regime; as a result, the energy dissipated in the vicinity of roughness ($(y-d)^+ \lesssim 10$) is mostly generated at the same wall-normal location (shown by the approximate equality of production and dissipation in this region in Fig. 11 (a)).

Quadrant analysis is also carried out. Following Wallace *et al.*[45], the averaged Reynolds shear stress is decomposed into contributions from four quadrants,

$$\langle u'v' \rangle_Q(y,H) = \langle u'(x,y,z)v'(x,y,z)I_Q(x,y,z,H) \rangle_{x,z}, \tag{14}$$

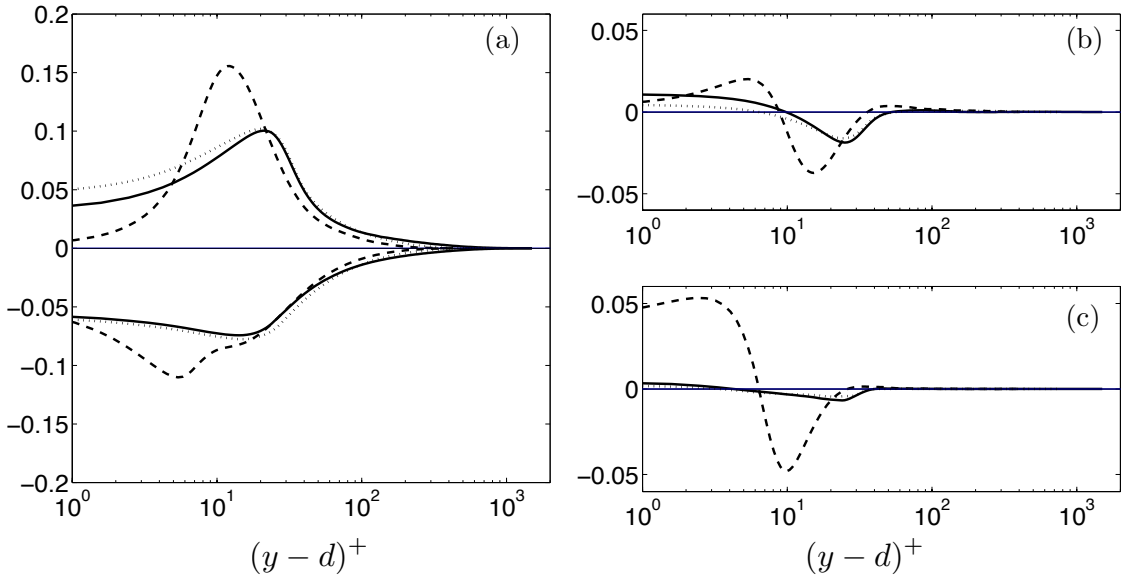

FIG. 11. Energy budgets of cases K1R1 (——), K3R1 (- - -), K3R3 (····). (a) Production and viscous dissipation, (b) turbulent diffusion and (c) viscous diffusion.

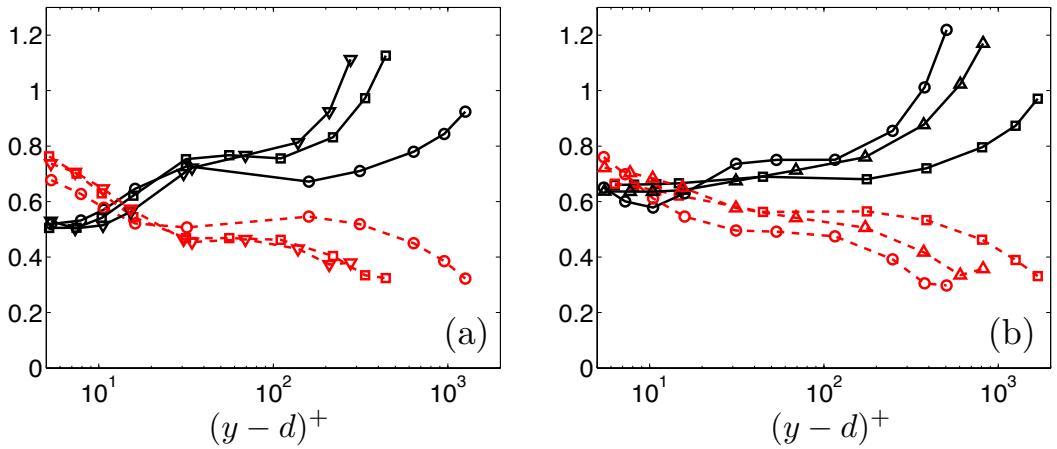

FIG. 12. Quadrant contributions from Q2 (——) and Q4 (- - -) events in (a) smooth cases K1R0 (◯), K3R0 (□), K4R0 (▽) and (b) rough cases K1R1 (□), K3R1 (◯), K3R3 (△).

where I_Q is an indicator function defined as

$$I_Q(x,y,z,H) = \begin{cases} 1 & \text{if } |u'v'|_Q(x,y,z) \geq H\sigma_{u'}(y)\sigma_{v'}(y), \\ 0 & \text{otherwise,} \end{cases} \tag{15}$$

and $\sigma_{u'}(y)$, $\sigma_{v'}(y)$ are the root-mean-square deviations of u' and v'. H is the strength threshold for the quadrant events to be considered. In all the cases, the contribution of the total sweeping (Q2) and ejecting (Q4) events, with $H = 0$, is $3-5$ times larger (in magnitude) than the contribution of the other two quadrants; therefore attention is given to

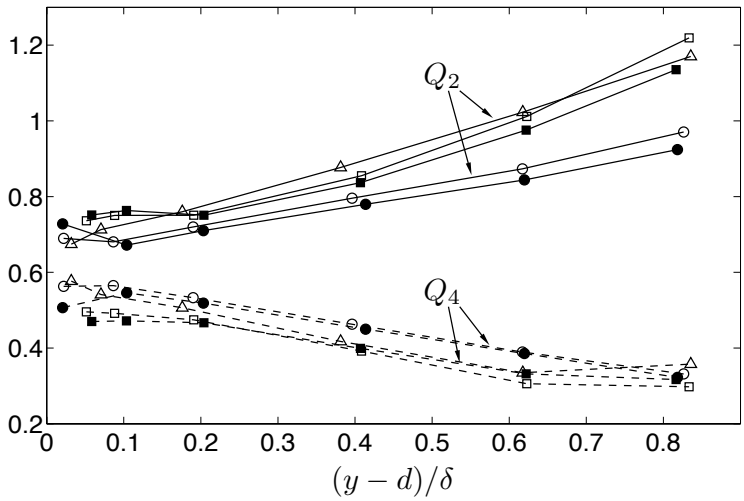

FIG. 13. Quadrant contributions from Q2 and Q4 events versus the wall-normal location in outer scaling. Smooth cases: K1R0 (filled ◯), K3R0 (filled □); rough cases: K1R1 (◯), K3R1 (□), K3R3 (△).

Q2 and Q4. The wall-normal distributions of the quadrant contributions are compared for the smooth cases [Fig. 12(a)] and three rough cases [Fig. 12(b)]. The smooth case resembles non-accelerating flows[46]: sweeps are more significant in the near-wall region and ejections in the outer flows, respectively, with the equal contributions occurring around $y^+ \approx 15$. Increase of K on both smooth and R1 rough walls shows that the main effect of K is to promote the Q2 contributions and to decrease those of Q4 in the region $(y-d)^+ > 20$. Less difference in the near-wall region is observed. Profiles of K3R1 and K3R3 show that an increase of $\overline{k}$ tends to restore the contributions in the region $15 \lesssim (y-d)^+ \lesssim 50$; near the wall, Q2 contributions from the rough cases are generally 30% higher than on a smooth wall. The role of roughness in intensifying ejections close to the wall and sweeps in the outer layer was also observed in experiments[5,47]. In Fig. 13, the wall-normal location is normalized using δ. For $(y-d)/\delta \gtrsim 0.2$, the rough-wall profiles fall on the respective smooth-wall profile with the corresponding K, indicating that the outer-layer similarity also applies to stress contribution of total Q2 and Q4 quadrant events.

C. Mean-flow structures

Roughness induces mean-flow heterogeneity near the wall, shown by $\widetilde{U}$ and $\widetilde{V}$ contours from Case K3R3 at $y = d$ in Fig. 14. Recall that $\widetilde{U}$ and $\widetilde{V}$ are the differences between time- and space-averaged velocities and the time-averaged ones. The velocities are normalized by u_τ. Comparing Fig. 14 (a) and (b), two types of motions can be identified: the mean sweeping motions, which appear as long streaks of positive $\widetilde{U}$ and negative $\widetilde{V}$, and the nearly vertical ejection motions, *i.e.*, regions of locally high magnitude of positive $\widetilde{V}$. The sweeping motions may be related to the mean-flow "channeling phenomenon" observed on pyramid roughness by Hong *et al.*[48]. In addition, Fig. 14 (c) shows the mean spanwise motions of the flow bypassing a single roughness element or a block of elements.

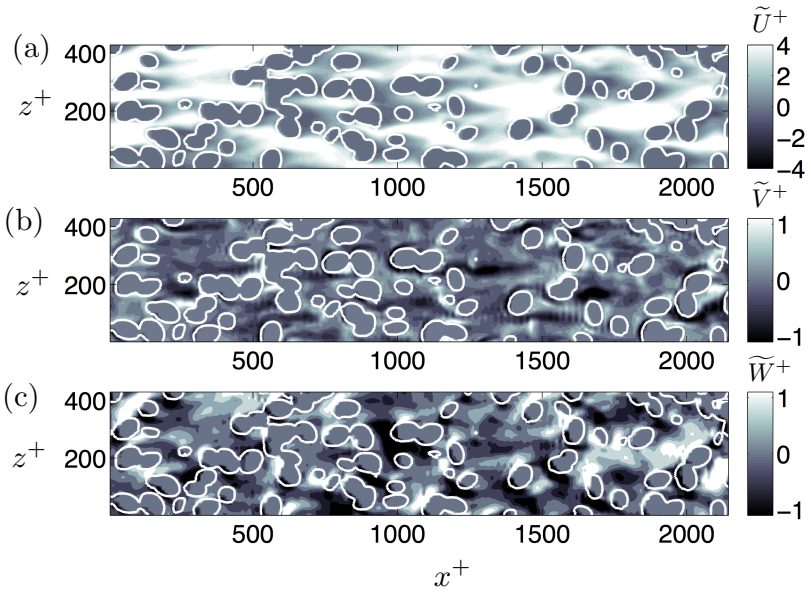

FIG. 14. Contours of (a) streamwise, (b) wall-normal, and (c) spanwise time-averaged mean flow in the (x, z) plane $y = d$ for case K3R3, normalized by u_τ and δ_ν.

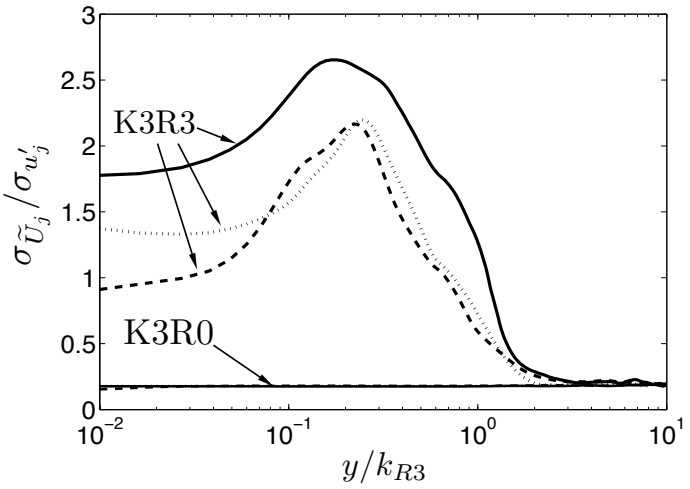

FIG. 15. Root-mean-square of time-averaged velocity for cases K3R0 and K3R3 normalized by the root-mean-square of the local turbulent fluctuation in the respective direction. k_{R3} is the roughness height for group R3.

The magnitude of the mean-flow heterogeneity versus the wall-normal direction is studied by considering the RMS of the mean-flow variation, $\sigma_{\widetilde{U}_j}(y)$, at each y location in Fig. 15. For $y < k$, the variation of $\widetilde{U}_j$ is stronger than that of u'_j, while for $y > 3k$, a plateau of minimum $\sigma_{\widetilde{U}_j}/\sigma_{u'_j}$ is reached. The non-zero value of $\sigma_{\widetilde{U}_j}$ in the outer layer is due to the limited temporal sampling of the flow, as is shown by the non-zero $\sigma_{\widetilde{U}_j}/\sigma_{u'_j}$ in the smooth case K3R0. Given that the thickness of the roughness sublayer is $5k$ for current roughness, the layer of significant mean-flow heterogeneity ($y/k < 3$) is inside the roughness sublayer.

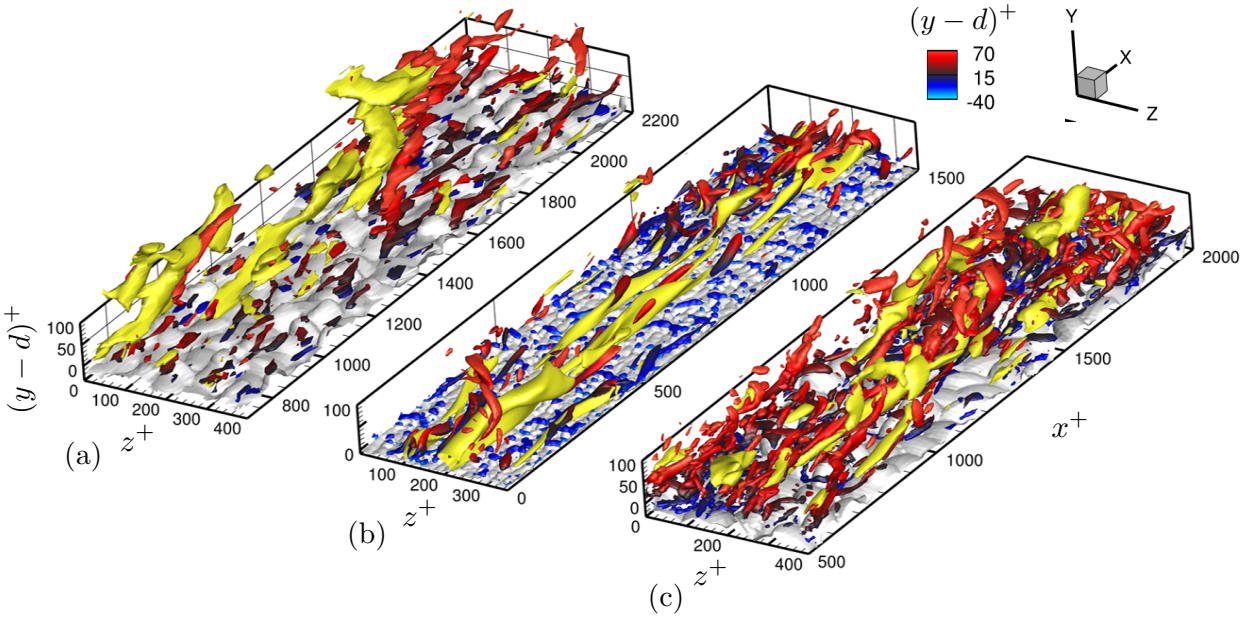

FIG. 16. Isosurfaces of $u'^+ = -3$ (yellow) and $Q^+ = 0.01$ (coloured by $(y-d)^+$) in cases (a) K1R1, (b) K3R1 and (c) K3R3. Rough surfaces are shown in white.

D. Near-wall turbulent structures

The turbulent vortices, shown by the isosurfaces of the second invariants of the full-velocity tensor

$$Q = -\frac{1}{2}\frac{\partial u_j}{\partial x_i}\frac{\partial u_i}{\partial x_i}, \tag{16}$$

and the low-speed regions, shown by the isosurfaces of $u'^+ = -3$, are presented in Fig. 16 for cases K1R1, K3R1 and K3R3. In all cases, the distribution and density of near-wall vortices closely correlate with the distribution of roughness elements. In case K3R1, two types of near-wall vortices are clearly identifiable: the roughness-scale vortices attached at the tip of the rough elements, and the vortices elongated in the streamwise direction, similar to the quasi-streamwise vortices over a smooth wall. The latter are mostly decorrelated from the roughness distribution; the low-speed regions are stable for a very long streamwise distance, usually from $700\delta_\nu$ to $1000\delta_\nu$, a feature similar to the low-speed streaks over a smooth wall. In the cases with $k^+ \approx 40$, the attached eddies extend into the layers of quasi-streamwise vortices; these quasi-streamwise vortices are more densely distributed compared to case K3R1; the low-speed regions are more limited in their streamwise lengths, usually $200 - 300\delta_\nu$, and are lifted up frequently upstream of a relatively tall roughness elements. Similar to the experimental observations of coherent structures in a fully-rough channel flow with pyramid roughness by Talapatra *et al.*[49], the prevalent structures in the two higher-k^+ cases are densely-distributed low-laying spanwise and groove-parallel vortical structures of the scale of the roughness, as well as quasi-streamwise vortices. The near-wall structures do not completely match the experimental observations due to the lower roughness Reynolds number and the randomness of roughness rotation and location. In the region $(y-d)^+ \gtrsim 50$, hairpin vortices are observed in in cases K3R1 and K3R3; the hairpins in case K1R1 mostly

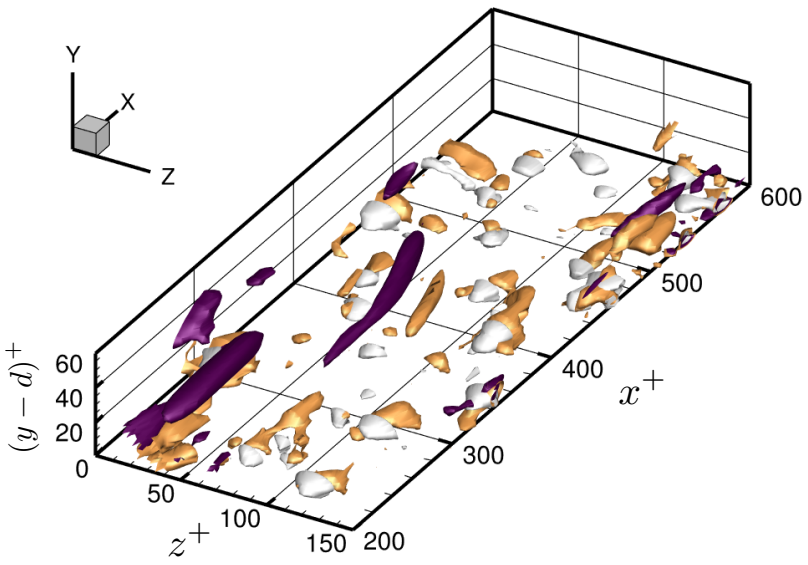

FIG. 17. Isosurfaces of components of Q: mean-flow component (white), turbulent component (purple), and the component corresponding to mean-flow and turbulence interaction (yellow).

appear above the region visualized, which is limited to the region $(y-d)/\delta < 0.05$, where the dominant structures are tilted, quasi-streamwise vortices.

To classify the near-wall vortices, Q is separated into three components,

$$Q = -\frac{1}{2}\frac{\partial(\widetilde{U}_j + U_j)}{\partial x_i}\frac{\partial(\widetilde{U}_i + U_i)}{\partial x_j} - \frac{1}{2}\frac{\partial u'_j}{\partial x_i}\frac{\partial u'_i}{\partial x_j} - \frac{\partial(\widetilde{U}_j + U_j)}{\partial x_i}\frac{\partial u'_i}{\partial x_j}, \tag{17}$$

where the terms on the right-hand-side are, from left to right, the contribution from near-wall mean-flow heterogeneity, the contribution from turbulence, and the component due to the interaction between mean flow and turbulence. The isosurfaces of all components are plotted in Fig. 17; the case K3R1 is chosen as an example due to the clear separation of these components. It is found that the attached roughness-scale eddies are due to mean-flow separations: they are either mean-flow eddies, or turbulent vortices that exist in the regions of high mean-flow gradient due to roughness. These eddies contribute to the differences of flow structures between smooth- and rough-wall flows. The wall-normal extension of the attached eddies depends on the height of roughness. For case K3R1, these eddies are mostly restricted to the region $y^+ < 14$, where viscous effects are significant, whereas in K3R3 and K1R1, they extend into the layer that is important for turbulent production, and lead to more densely distributed quasi-streamwise vortices, probably because they augment streaks instability. Such roughness effect is consistent with earlier observations that the near-wall Reynolds-stress anisotropy and TKE budgets satisfy similarity for cases with the same k^+, since k^+ is the ratio between the physical roughness height and the thickness of the layer where viscosity is important.

To compare quantitatively the size and inclination of the near-wall turbulent structures, Fig. 18 shows the two-point correlations of streamwise fluctuations, R_{uu}, in the (x, y)-plane centred on $y = k$, for the three cases. R_{uu} at a reference wall-normal location, y_{ref}, is defined

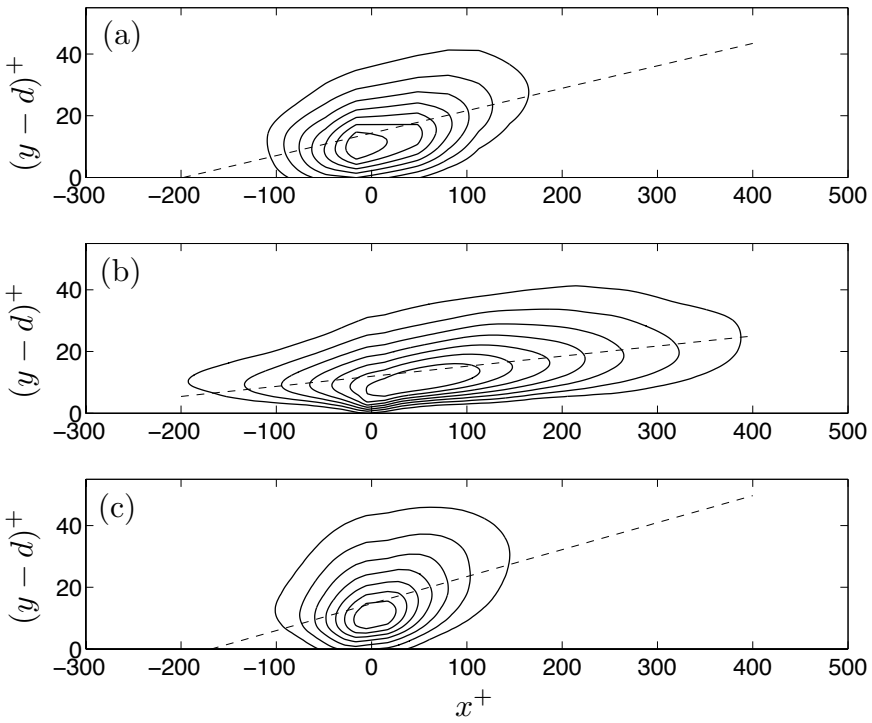

FIG. 18. Two-point correlations of streamwise fluctuations, R_{uu}, centered on $y = k$. Contour levels: from 0.3 to 0.9 with increment 0.1. Cases (a) K1R1, (b) K3R1, and (c) K3R3 are shown.

as

$$R_{uu}(\Delta x, \Delta y, y_{\text{ref}}) = \frac{\langle u'(x, y_{\text{ref}}, z)\ u'(x + \Delta x, y_{\text{ref}} + \Delta y, z)\rangle}{\sigma_{u'}(y_{\text{ref}})^2}, \tag{18}$$

where Δx and Δy are separations in the streamwise and the wall-normal directions. Following Volino *et al.*[41], the inclination angle is obtained from the line fitted using the least-square method from points farthest upstream and downstream from the correlation peak on each of the contour levels from 0.4 to 0.9 with increment 0.1. A decrease of k^+ (from K1R1 and K3R3 to K3R1) leads to more elongated near-wall coherent structures in the streamwise direction, and the wall-normal dimension becomes more limited; as a results, case K3R1 exhibits a shallower inclination (3°) compared to case K1R1 (13°) and case K3R3 (10°). This phenomenon can be explained by larger streamwise coherence due to less frequent lift-ups of low-speed streaks and a decrease of bursting.

To study the variation of large-scale structure size against the wall-normal location, Fig. 19 compares the integral length scales, defined as

$$L_{\alpha\beta}(y) = \int_0^\infty R_{u_\alpha u_\beta}(y, \Delta r) d(\Delta r), \tag{19}$$

where $R_{u_\alpha u_\beta}$ is the two-point spatial correlation in the (x, z)-plane, defined as

$$R_{u_\alpha u_\beta}(y, \Delta r) = \frac{\langle u'_\alpha(y, r) u'_\beta(y, r + \Delta r)\rangle}{\sigma_{u'_\alpha}(y)\sigma_{u'_\beta}(y)}, \tag{20}$$

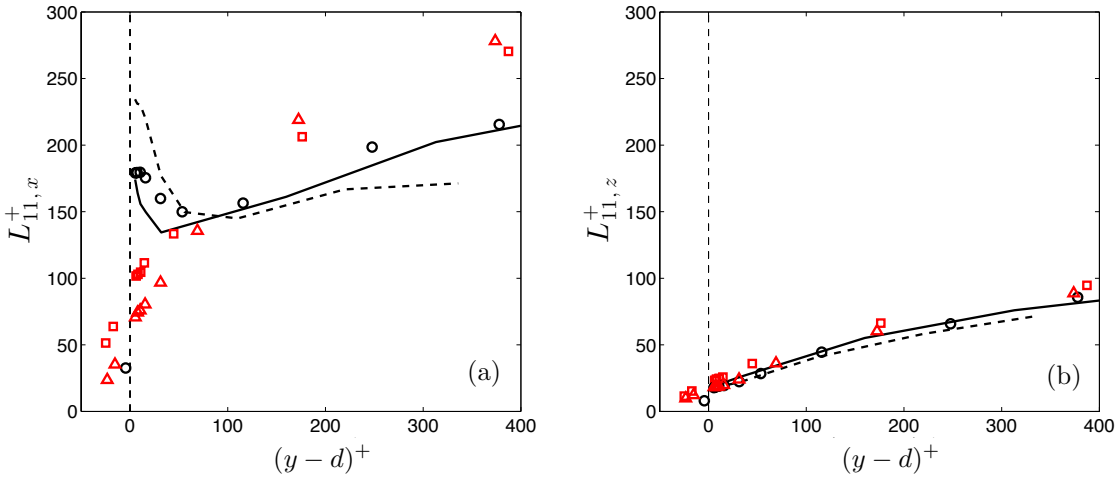

FIG. 19. Integral length scale in (a) the streamwise and (b) spanwise directions in inner scaling. —— K1R0, - - - K3R0, □ K1R1, ◯ K3R1, △ K3R3.

and r denotes the location in x (for $L_{\alpha\beta,x}$) or z (for $L_{\alpha\beta,z}$). To remove errors due to fluctuations in the two-point correlation caused by insufficient sample, the integration is carried out to the value of Δr at which the correlation coefficient first crosses 0.2. $L^+_{11,x}$ in both two smooth cases and case K3R1 presents a peak in the wall region due to the flattening and elongation of near-wall structures; it then decreases slightly. Qualitatively similar trends were observed in experimental smooth-wall sink-flow studies[34]. In the rough cases with higher k^+, $L^+_{11,x}$ is quite different: cases K1R1 and K3R3 almost collapse and produce a monotonically increasing $L^+_{11,x}$. The effects of K and $\overline{k}$ on the spanwise integral length are absorbed into the viscous length scale.

E. Outer-layer turbulent structures

Hairpin vortices, either symmetric, asymmetric, or one-sided, are frequently observed in the outer layer (Fig. 16 (b), (c)). The visualizations of velocity vectors in Fig. 20 using the approach of Adrian *et al.*[50] demonstrate the existence of the hairpin packets, shown by the shear layer separating the low-speed and high-speed region, and by the chains of negative-ω_z regions, which can be interpreted as hairpin heads. In all three cases, the inclinations of the packets are around $12° - 14°$ and the packet extensions are around 1δ, insensitive to either acceleration or roughness. The inclination of the local shear layer upstream of a single hairpin varies widely, often from 30° to 65°, and its value range is not significantly different from case to case; the average separation between hairpins in a packet varies from case to case in Fig. 20 when normalized by δ, but, under inner scaling, they are all around 100–150 wall units. These observations of hairpin structures and packets are consistent with experimental observations in ZPG turbulent boundary layers[50]; no significant change is caused by either roughness or acceleration.

The size and inclination of the packets is shown by the contour of two point correlation of u' (Fig. 21). The inclination angles, obtained using the same fitting approach in Fig. 18, vary weakly in all three cases (Fig. 21 (a)–(c)) and in a case with higher K (K4R3, Fig. 21

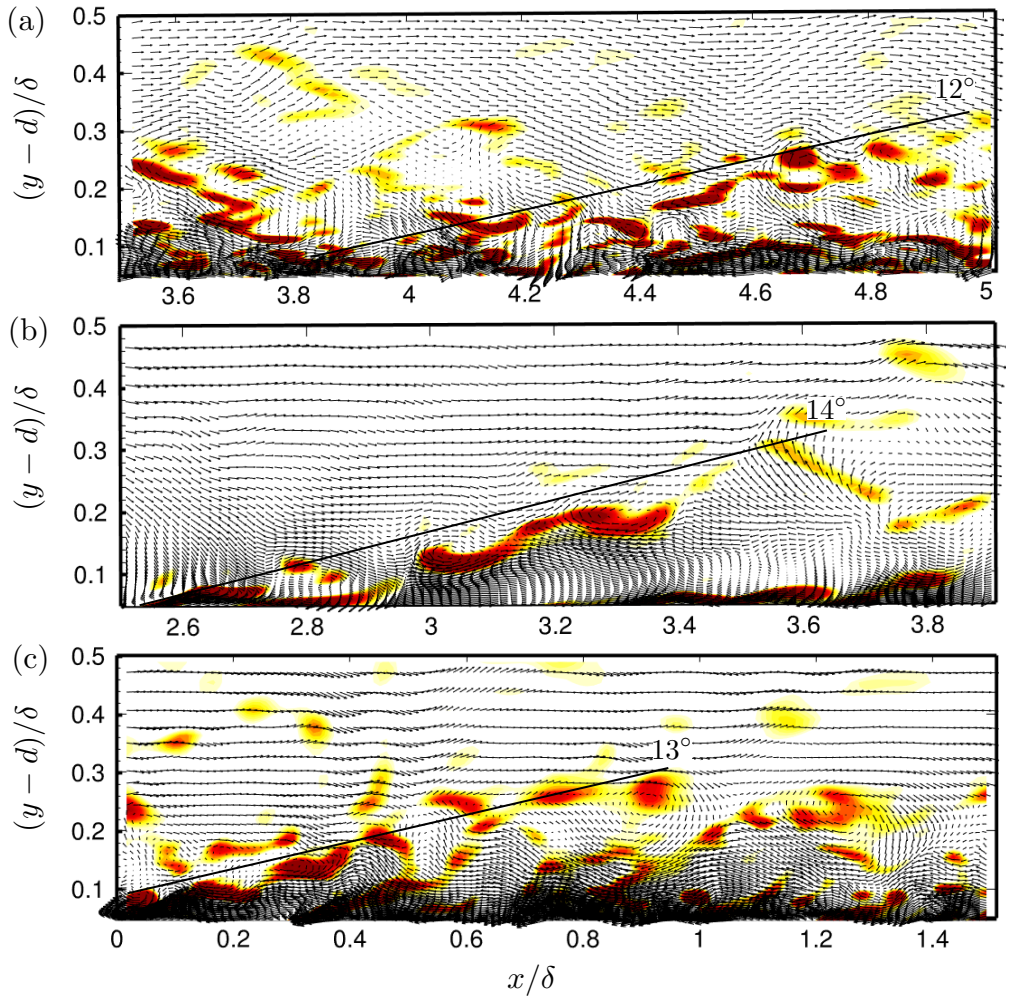

FIG. 20. Instantaneous velocity vectors and contours of negative ω_z in case (a) K1R1, (b) K3R1, (c) K3R3. The convection velocity $U_c = 0.8U_\infty$ is subtracted from the velocity field. Lines indicate angles of hairpin packets. Contour level: $-5.7 \leq \omega_z\delta/U_\infty \leq -0.8$. Every other grid point in x and y directions is used for plotting velocity vectors.

(d)), from $10^\circ - 12^\circ$, within the 10°–15° range obtained in many former experimental and numerical studies of ZPG turbulent boundary layers and channel flows.

In smooth-wall sink flows, Dixit and Ramesh[34] associated the decrease of hairpin-packet inclination angle to the reverse-transition; they obtained the inclination of overall near-wall structures from the location of maximum cross-correlation between wall-shear stress and u' in the region $0.1\delta < y < 2.5\delta$, and found that an increase in K from 0.77×10^{-6} to 1.74×10^{-6} weakly decreases the structure inclination by 20%. It is interesting, however, that here K is shown to exert no visible effect in transitionally-rough sink flows, even when $K = 2.5\times10^{-6}$ (case K4R3), which, in the case of a smooth-wall, would lead to nearly relaminarized flow, and much smaller inclination angle.[34]

On the role of roughness on outer-layer structure inclination, weak roughness effects were observed in a number of experimental studies, *e.g.*, by Volino *et al.*[41], where the inclinations on rough-wall ZPG boundary layers fall in the $10^\circ - 15^\circ$ range, consistent with the current

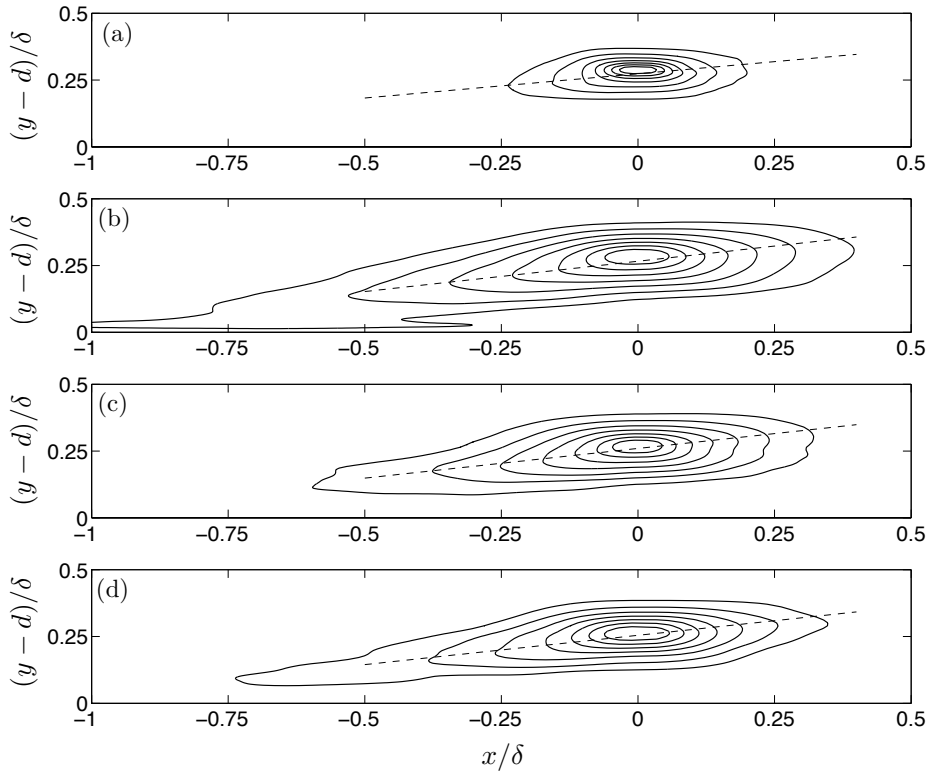

FIG. 21. Two-point correlations of streamwise fluctuations, R_{uu}, centered on $y = 0.3\delta$ in fully turbulent rough-wall cases: (a) K1R1, (b) K3R1, (c) K3R3, (d) K4R3. Contour levels: 0.3 to 0.9 with increment 0.1.

study. However, a significant role of roughness in increasing outer-layer structural inclination was observed in several experimental studies, *e.g.*, Krogstad and Antonia[51], and in DNS studies by Lee *et al.*[20], on ZPG boundary layers; this may be due to the higher blockage ratio k/δ, since a necessary condition for the outer-layer similarity in rough-wall turbulence is a significant separation between the roughness length scale k and the boundary layer thickness.[4]

The correlation contours in Fig. 21 also show an increase of structure size as K increases. In case K3R1, the increase in the dimension of the eddies results in connections between the hairpin packets and the near-wall structures upstream (from $x/\delta = -1.0$ to -0.5 in Fig. 21 (b)); this phenomenon, however, is not observed in case K3R3 (Fig. 21 (c)). This indicates that, in case K3R3, the hairpins in the outer layer are decorrelated with the structures in the region directly affected by the randomly-distributed roughness; these structures include the legs of primary hairpins whose heads have already evolved into the outer layer, and any secondary hairpin they generate from the legs.

Figure 22 compares the integral length scales defined in Eq. (19), normalized by δ, in the streamwise and spanwise directions. Both $L_{11,x}$ and $L_{11,z}$ in the outer layer cluster into two branches that differ in acceleration level. This indicates that acceleration dominantly determines the scales of the largest structures in the outer layer: a stronger acceleration leads to a larger size of the outer-layer structures. This may be explained by the "pure-wall-flow" nature of a sink flow, in which the outer-region structures also scale with the viscous

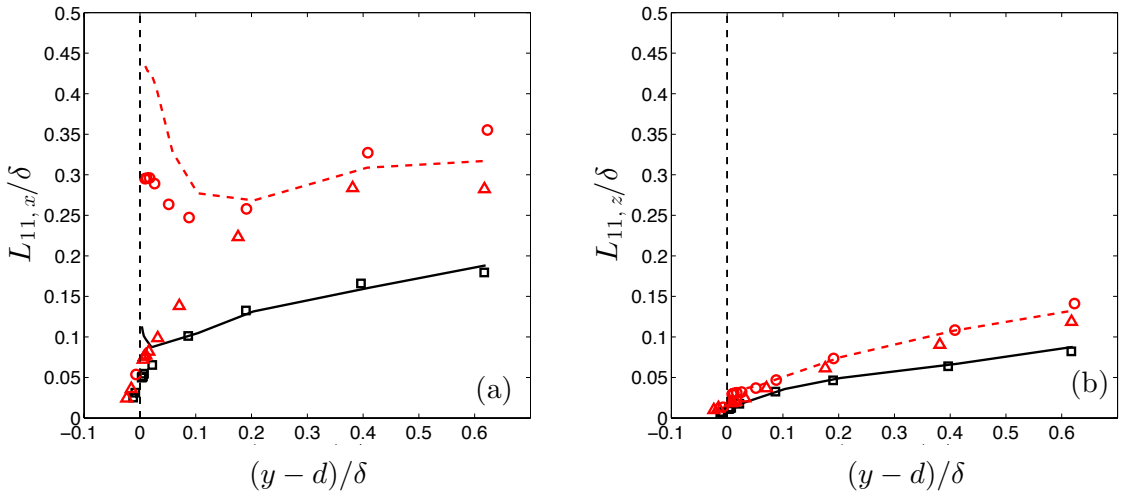

FIG. 22. Integral length scale in (a) the streamwise and (b) spanwise directions in inner scaling. —— K1R0, - - - K3R0, □ K1R1, ◯ K3R1, △ K3R3.

length scale. Increasing from K1 to K3 results in almost 100% increase of the outer-layer $L_{11,x}/\delta$ (Fig. 22 (a)), while, when plotted in wall units, it reduces to a 15% increase in $L^+_{11,x}$ (Fig. 19 (a)); if the cut-off value of R_{uu} for calculating the integral length is changed to 0.5, $L^+_{11,x}$ can be shown insensitive to K outside of the roughness sublayer. The roughness effect is negligible in the outer layer; but the roughness decreases the streamwise integral length scale in the roughness sublayer, and the amount of decrease is augmented by a higher $\overline{k}$. The decrease of size of large structures near the wall for the sand-grain (SG) roughness agrees with experimental observations on three-dimensional mesh roughness by Volino *et al.*[41], while it is opposite to the increase of the streamwise extent of R_{uu} observed throughout the boundary layer over two-dimensional bars[10] and in the roughness sublayer above a type of realistic roughness[11].

The correlation between strong quadrant events and the turbulent structures in the outer layer is shown in Figure 23. Compared to Q4 events, the distribution of Q2 events relates much more closely to the hairpin heads: strong Q2 events with $H \geq 1$ are present below and immediately upstream of the hairpin heads. The Q4 events distribute widely outside of the region enclosed by the hairpins. For $H = 1$, the Q4 events occupy larger total area compared to Q2 events, but Q2 events reach much higher strength than Q2; as a result, Q2 events contribute more than Q4 events to the averaged Reynolds shear stress at this elevation.

The good correlation between the patches of strong Q2 events and the hairpin structures allows us to study the density of the outer-layer turbulent structures. Note that the notion of "structure density" in space is in analogy to the "bursting frequency" in time, which is widely used by experimentalist in analyzing turbulent structures. The quantification of a burst event includes the burst size, denoted by A, and the mean separation between two events, r. The burst intermittency (or "space ratio"), γ, defined as the ratio between the total event area and the total domain area, quantifies the strength of turbulent production. Various detection techniques have been used in the literature to identify bursts; reviews of major methods can be found in Robinson[52] and Bogard and Tiederman[53]. Bogard and Tiederman[53] concluded that the $u'v'$ quadrant method[45] is less prone to false detection. Here the quadrant technique is also employed; specifically, a burst event is considered to be

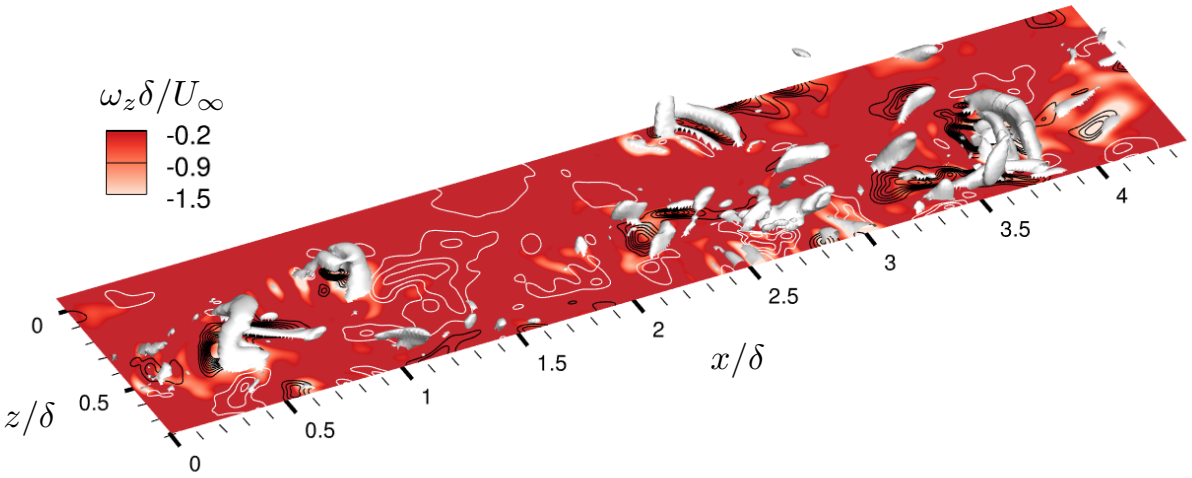

FIG. 23. Contour lines of $u'v'|_{Q2}$ (black) and $u'v'|_{Q4}$ (white) induced by the hairpin structures (isosurfaces of $QX_o/U_{\infty,o} = 800$) in Case K3R3. Plane located at $(y-d)/\delta = 0.5$. Contour of negative $\omega_z\delta/U_\infty$ shows hairpin heads. Contour line levels: from $\sigma_{u'}\sigma_{v'}$ to $20\sigma_{u'}\sigma_{v'}$ with increment $\sigma_{u'}\sigma_{v'}$.

a strong ejection corresponding to values of H equal to 1, 2, and 4. The threshold value $H = 1$ was found to provide the highest percentage of ejections detected,[53] while higher H are also used to study stronger events, although only a subset of them is detected.

The intermittency γ is calculated by counting the grid cells with $|u'v'|_{Q2}(x,y,z)$ stronger than the threshold. To quantify A, first, for a (x,z)-plane, a masked field of relatively strong Q2 stress, $u'v'|_{Q2}$, is obtained as

$$u'v'|_{Q2}(x,y,z,H) = u'(x,y,z)v'(x,y,z)I_{Q2}(x,y,z,H). \tag{21}$$

Then the two-point auto-correlation, $R_{QQ,st}$, of the marked field is calculated as

$$R_{QQ}(\Delta x,\Delta z,y,H) = \frac{\langle u'v'|_{Q2}(x,y,z,H)\ \ u'v'|_{Q2}(x+\Delta x,y,z+\Delta z,H)\rangle}{\sigma^2_{Q2}}, \tag{22}$$

where σ_{Q2} is the standard deviation of $u'v'|_{Q2}$ in the corresponding (x,z)-plane. A is then obtained as the averaged area of coherent ejection events,

$$A(y,H) \equiv \iint\limits_{R_{QQ}\geq 0.1} R_{QQ}(\Delta x,\Delta z,y,H)\ \mathrm{d}\Delta x\,\mathrm{d}\Delta z, \tag{23}$$

where the value 0.1 is used as it is effective in capturing the size variation. r can then be defined as

$$r(y,H) \equiv \sqrt{\frac{A(y,H)}{\gamma(y,H)}}. \tag{24}$$

The intermittency and period (T_b) of bursts in smooth-wall sink flows were studied in experiments by Chambers *et al.*[54]; detection was made when the local variance of wall-shear

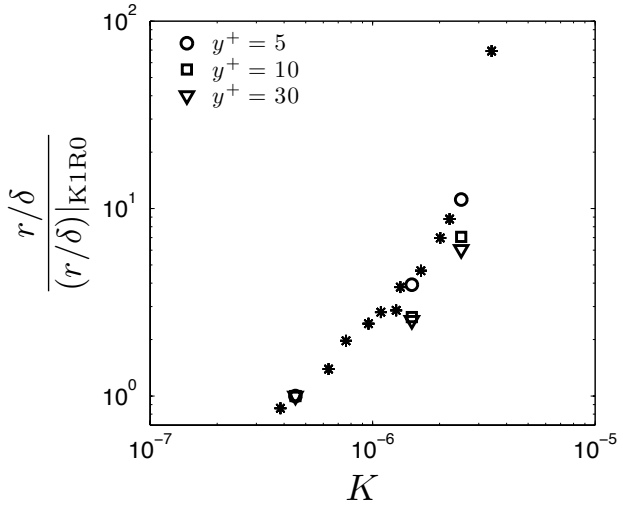

FIG. 24. Averaged separation (inverse of density) of Q2 events detected with $H = 1$ at different near-wall elevations in smooth cases. $*$ Chambers *et al.*[54] experiment.

stress exceeded a critical value, with the threshold chosen by matching their detection with Blackwelder and Kaplan[55] in their boundary-layer studies, where the detection is based on the local velocity variance that is higher than 1.2 times of the variance obtained from short-term average, at the elevation $y^+ = 15$. To validate the current approach, we compare our smooth-wall results with Chambers *et al.*[54]; the experimental results are treated using Taylor hypothesis with the assumption that, near the wall, the event convection velocity, U_C, varies linearly with u_τ,

$$r_{\mathrm{exp}} = T_b U_C \sim T_b u_\tau,$$

where the subscript "exp" indicates data from experiments. The response of near-wall r in current smooth-wall cases (K1R0, K3R0, K4R0) are compared with r_{exp} in Fig. 24 with $H = 1$. Here a low H value is used to detect a high percentage of bursts. A range of near-wall locations from $y^+ = 5$ to 30 is considered. All data points are normalized with the corresponding value in case K1R0. All current data follow closely with the growth of r_{exp}, and it is not surprising to find that the most near-wall data best match the experimental results obtained with the signal of wall-shear stress. The relatively strong Q2 events at $y^+ = 5$ represent the kinks of the low-speed streaks, which have been shown to be frequently the early stage of secondary hairpin vortices.[56]

Figure 25 (a) shows the effects of roughness and acceleration on the average separation (*i.e.*, the inverse of density) of the coherent turbulent structures: acceleration significantly decreases the density (or increases r) throughout the boundary layer. Roughness, on the other hand, causes more frequent appearance of structures close to the wall, but does not affect the outer layer ($(y-d)/\delta > 0.2$). The spatial intermittency of the events (Fig. 25 (b)), as a product of event density and event size, is not significantly affected by acceleration, despite a slightly decrease in the outer layer; this is because, although acceleration decreases the number of coherent structures, the size of the structures becomes larger (shown by the increases of integral length scales in Fig. 22). Roughness has no significant effect on γ in the outer layer, consistent with experimental observations by Wu and Christensen[11]. Varying H from 1 to 4, we found that the effects of the threshold value to the above outer-layer

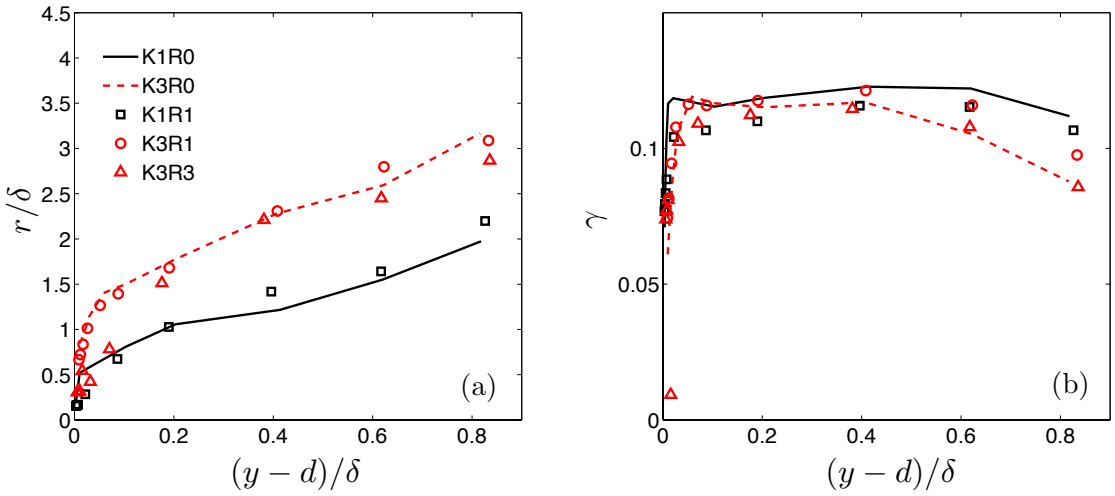

FIG. 25. (a) Averaged separation and (b) intermittency for strong Q2 events with $H = 1$ in cases K1R1, K3R1, and K3R3, compared to corresponding smooth cases.

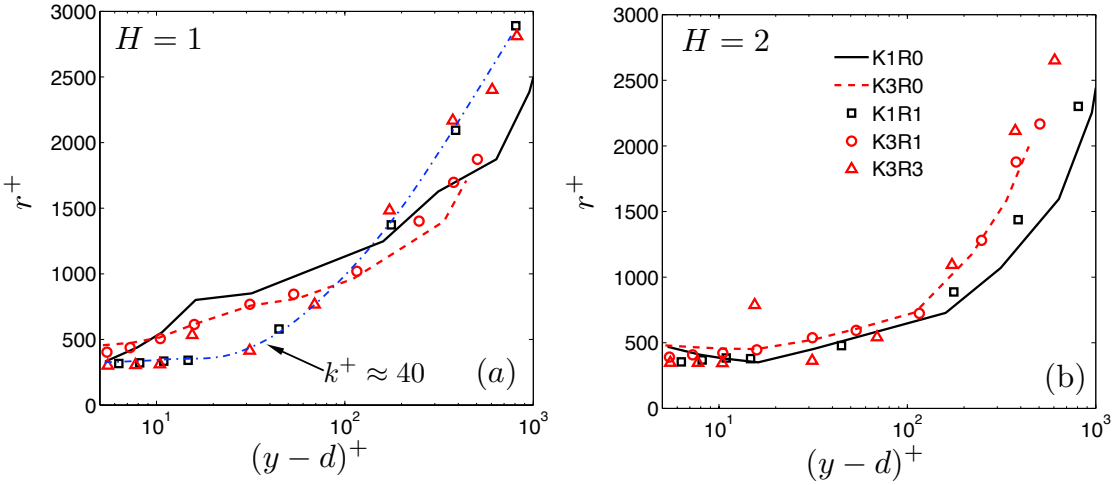

FIG. 26. Averaged separation of strong Q2 events in case K1R1, K3R1, and K3R3 in inner scaling: (a) $H = 1$, - - - : cases with $k^+ \approx 40$; (b) $H = 2$.

observations are minimum.

When the structure density is plotted in inner scales (Fig. 26 (a)), the cases collapse onto two profiles: the low-k^+ case collapse with the two smooth cases; the high-k^+ cases show much lower r^+ compared to the cases with low or no roughness in the region $5 < (y-d)^+ < 100$. This means that structure density also follows the k^+-based similarity; a higher k^+ leads to more frequent near-wall events with strength $|u'v'|_{Q2} > \sigma_{u'}\sigma_{v'}$. This phenomenon was also observed earlier from near-wall structure visualization (Fig. 16), where the number of quasi-streamwise vortices are distributed more densely in cases with higher k^+. However, for higher threshold values, such as $H = 2$ (Fig. 26 (b)) or $H = 4$ (not shown), the density in the near-wall region is the same on both smooth and rough walls. Thus, roughness increases the number of relatively weak turbulent structures, but not those strong enough to result in

Q2 events with $|u'v'|_{Q2} > 2\sigma_{u'}\sigma_{v'}$.

IV. CONCLUSIONS AND DISCUSSIONS

Large-eddy and direct numerical simulations are carried out for equilibrium sink flows over a smooth wall or sand-grain roughness. The acceleration parameter, K, and the normalized roughness height, $\overline{k}$, are parameters quantifying the acceleration and roughness effects. The roughness Reynolds number k^+ can be used as an indicator of the relative strength of these two effects.

Acceleration is found to decrease Re_θ and C_f, while roughness increases both. When k^+ is kept constant, Re_θ and C_f are dominantly affected by K and $\overline{k}$, respectively. Roughness tends to prevent the reverse-transitional state (characterized by a significant decrease of the log-law slope), which occurs only when the flow is close to the hydraulically smooth regime and subjects to a strong acceleration (K4). In the fully turbulent state, the roughness function depends on k^+ only, and agrees with experimental data obtained from equilibrium pipe flows with the same type of roughness.

Wall-similarity applies to the Reynolds stresses for cases far from the reverse-transitional state; when the flow is close to reverse-transition, u_τ does not absorb the effects of acceleration or roughness in a significant part of the lower boundary layer. In any case, a higher acceleration increases the peak of $\langle u'^2\rangle^+$ and decreases the peaks of $\langle v'^2\rangle^+$ and $\langle u'v'\rangle^+$, while a higher roughness exerts the opposite effects.

The statistics in the near-wall region exhibit similarity based on k^+: cases with higher k^+ show more homogeneous distribution of energy in three components of turbulent fluctuations and higher Reynolds shear stress $\langle u'v'\rangle^+$; the production of turbulent kinetic energy peaks farther away from the wall, and is mostly balanced by local viscous dissipation, with negligible viscous diffusion and weaker turbulent diffusion. The similarity also applies to turbulent structures: as k^+ increases, their average inclination becomes steeper, the streamwise size of near-wall turbulent structures decreases, and the relatively weaker Q2 events (with strength lower than $2\sigma_{u'}\sigma_{v'}$) appear more frequently. This is because k^+ is a ratio of the physical roughness height to the thickness of the viscous layer; for high k^+, the hairpin packets near the wall are shorter and distributed more uniformly in the (x, z)-plane, presumably due to the inability of an initial hairpin to form secondary hairpins that are aligned with itself in the streamwise direction, as the randomly-distributed roughness directly affects the evolution of hairpin legs, where the secondary hairpins are often formed. The higher structure density is also due to the fact that a higher k^+ augments the magnitudes of v'^+ and w'^+, both of which have been shown to play an important role in streak instability.[57,58] The role of K comes in by decreasing k^+, reducing the impact of roughness on hairpin development, and thus increasing the streamwise packet length; effectively, the average packet inclination angle decreases.

In the outer layer, wall-similarity applies to transitionally rough cases in the Reynolds stresses, and in the statistics of turbulent structures including average inclination and size of hairpin packets, as well as their density. The disappearance of roughness effects in the outer layer may be because that, as the hairpins develop into this layer, their spanwise size increase, and the resultant hairpin-merging phenomenon absorbs the roughness-scale spanwise misalignment among hairpins, removing the effects of roughness on decreasing streamwise extents of hairpin packets. For the fully turbulent cases, K affects the outer-

layer flow mainly by increasing δ_ν/δ; as a result, the cases with stronger acceleration shows larger coherent structures compared to the boundary layer thickness, and less number of these structures in the domain.

It is interesting to observe that, unlike in a smooth-wall sink flow, a strong K does not necessarily lead to reverse transition in transitionally-rough sink flows; this is shown by the fact that an increase of K does not result in a decrease of the inclination angle of hairpin packets in the outer layer, which is considered the cause of reverse-transition in sink flows.[34] Instead, reverse transition occurs only when the flow is in the hydraulically-smooth regime and, at the same time, is subject to a strong acceleration. This finding supports the idea that acceleration-induced relaminarization starts from the near-wall region, and can be overruled by near-wall destabilization.[28]

ACKNOWLEDGMENTS

Support from Hydro Québec, the Natural Science and Engineering Research Council of Canada (NSERC), and the High Performance Computing Virtual Laboratory (HPCVL) is acknowledged. Professor Alberto Scotti is thanked for the code generating the volume fraction for the immersed boundary method.

Appendix A: Immersed boundary method

In the current fractional-step framework, the prediction step is carried out twice. Take DNS as an example; in the first step, a preliminary predicted velocity, $\widehat{u}'_j$, is obtained without F_j,

$$\left[1-\Delta t\frac{\partial}{\partial y}\left(\nu\frac{\partial}{\partial y}\right)\right]\widehat{u}'_j = u_j^n + \Delta t\left(\frac{3}{2}RHS^n - \frac{1}{2}RHS^{n-1}\right) + \frac{1}{2}\Delta t\frac{\partial}{\partial y}\left(\nu\frac{\partial u_j^n}{\partial y}\right), \quad \text{(A1)}$$

where RHS^n denotes the sum of convection, pressure, and the streamwise- and spanwise-viscous terms, at time step n. Note that the implicit time-advancement is applied to the wall-normal viscous term only. Then F_j is obtained as

$$F_j^n = -(1-\phi)\frac{\widehat{u}'_j}{\Delta t}. \quad \text{(A2)}$$

The second prediction step, in the same form as Eq. (A1), is then carried out with F_j^n and F_j^{n-1} as the source terms in RHS^n and RHS^{n-1}, and the final predicted velocity, $\widehat{u}_j$, is obtained. Note that, for LES, the eddy viscosity must also be reduced by $(1-\phi)$ to account for the decrease of sub-grid length scale. $\widehat{u}_j$ at the boundary cell is approximately reduced by $(1-\phi)$; the reduction of $(1-\phi)$ is exact, however, when explicit Euler time-advancement is used. This approach is similar to the one used by Scotti[18], who obtained $\widehat{u}_j$ by scaling directly $\widehat{u}'_j$ with the volume fraction without the second prediction step, *i.e.*, $\widehat{u}_j = (1-\phi)\widehat{u}'_j$, and used no explicit body-force term. The advantage of the current IBM, compared to the approach of Scotti[18], is that the explicit forcing terms can be integrated directly to obtain the total drag, f_d (described in Appendix C), bypassing the use of velocity and pressure

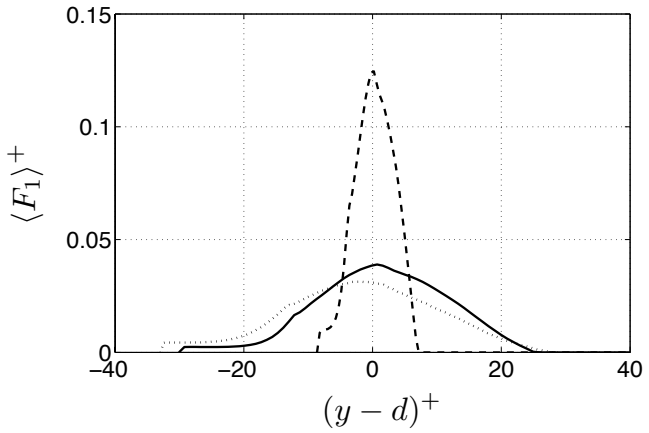

FIG. 27. Profiles of time- and space-averaged roughness body-force in cases K1R1 (——), K3R1 (- - -) and K3R3 (·····).

distributions, which are highly complicated due to surface-shape randomness. The forces are distributed in the boundary cells, and are zero inside the roughness.

Compared to direct-forcing methods, this method is simple to implement and does not depend on the discretization scheme. It does, however, lead to a diffused interface whose exact location is determined only to the order of the grid size. In the application studied here, the roughness length scale is large compared to the grid size; also, the flow around a particular roughness element is not of primary interest; thus, the grid-wise pixelation of the roughness surface does not systematically affect the structural statistics in the roughness sublayer.

Appendix B: Roughness forcing

The streamwise body force imposed by the immersed boundary method, $F_1(x, y, z, t)$, is non-zero only within the region physically occupied by roughness. Figure 27 shows the wall-normal distribution of the time- and space-averaged body force, $\langle F_1 \rangle(y)$. Normalized in wall units, the sum of the area below the curve is unity, since the integration of the forcing gives the total drag (Appendix C). The forcing peak occurs in the plane $y = d$; the higher the roughness elements, the more the forcing is spread; $\langle F_1 \rangle(y)$ reaches zero at the lower boundary of the domain (since $u = 0$ at $y = 0$), and at the maximum height of the rough surface.

The stress balance for case K1R1 is shown in Fig. 28, where the terms are obtained from integrating the equation of u-momentum conservation in the wall-normal direction from y to ∞, averaged in time and space,

$$-\langle (u' + \widetilde{U})(v' + \widetilde{V}) \rangle|_y = \int_y^\infty \left(\langle F_1 \rangle + \langle G_1 \rangle \right) \, dy - \nu \left. \frac{\partial U}{\partial y} \right|_y - \left. \langle \nu_T \frac{\partial u}{\partial y} \rangle \right|_y ; \qquad \text{(B1)}$$

the term on the left-hand-side is the Reynolds shear stress (calculated with respect to the deviation from the time- and space-averaged velocity, *i.e.*, $u'_j + \widetilde{U}_j$), and the terms on the right-hand-side are, respectively, the integrated roughness-forcing and growth terms, the

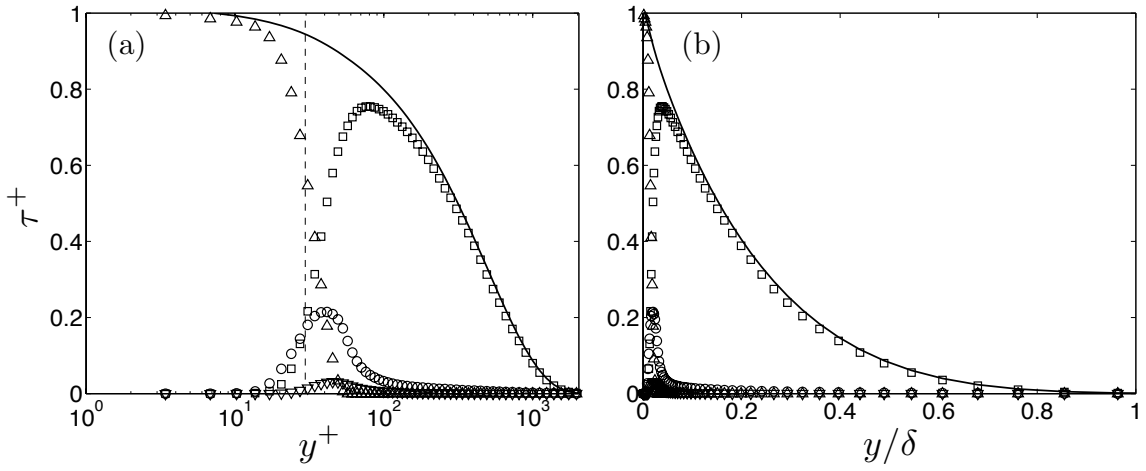

FIG. 28. Stress balance of case K1R1 against the wall-normal location (a) normalized by viscous length scale (--- $y^+ = d^+$) and (b) by boundary layer thickness. —— Growth term, △ roughness drag, □ Reynolds shear stress, ◯ viscous stress, ▽ subgrid-scale stress.

viscous stress, and the SGS stress; Note that $\partial\langle P\rangle/\partial x = 0$, the averaged flow is periodic in x and z, and that at $y = \infty$, the Reynolds shear stress, the viscous stress, and the SGS stress are all zero. Fig. 28 shows that the growth term plays the role of the pressure-gradient that balances the sum of the other stresses; the log-scale in Fig. 28 (a) zooms in to the near-wall region, showing that the roughness forcing is the only important term in most of the region below the roughness tip, and that the viscous stress is weak throughout the boundary layer, consistent with the fact that case K1R1 ($k^+ \approx 40$) is far from the hydraulically smooth regime.

Appendix C: Drag calculation

The sum of pressure and viscous drag on a rough surface at a given location and time is obtained as

$$f_d(x,z,t) = \int_0^\infty F_1(x,y,z,t)\,dy. \tag{C1}$$

To explain this approach, we consider the stress balance,

$$\int_0^\infty \langle G_1\rangle\,dy = -\langle f_d\rangle + \nu\,\frac{\partial U}{\partial y}\bigg|_0 - \langle(u'+\widetilde{U})(v'+\widetilde{V})\rangle\Big|_0 + \langle\nu_T\frac{\partial u}{\partial y}\rangle\Big|_0. \tag{C2}$$

At $y = 0$, the velocity magnitude is zero; the wall-normal velocity-gradient is negligible (since, in the vicinity of the domain bottom, roughness occupies most of the physical space, and thus the fluid is nearly static). Therefore, Eq. (C2) reduces to

$$\int_0^\infty \langle G_1\rangle\,dy = -\langle f_d\rangle,$$

i.e., $\langle f_d\rangle$ is the total drag of the surface. Note that $\langle f_d\rangle$ is negative, because $\langle F_1\rangle(y)$ is in the opposite direction of the mean flow (according to Eq. (A2)) and thus is negative for all y;

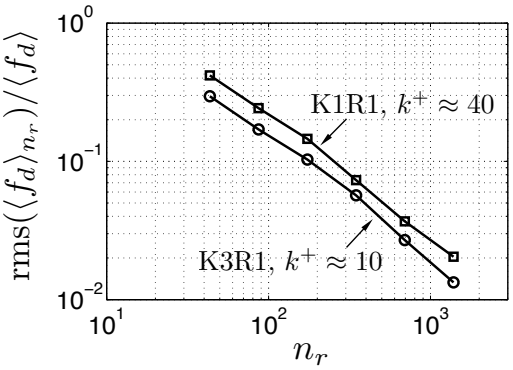

FIG. 29. Convergence of the root-mean-square of drag averaged from n_r roughness samples, $\langle f_d\rangle_{n_r}$, in two cases as n_r increases. $\langle f_d\rangle$ is the value averaged from 22311 samples.

however, the local $\langle f_d\rangle_t(x,z)$ can be either positive or negative depending on the direction of local time-averaged velocity in the vicinity of roughness.

Appendix D: Drag convergence with number of roughness elements

The distribution of f_d is affected by the randomness of the roughness distribution, in terms of location and rotation angle. Although rotation angles and location of the roughness elements satisfy an uniform distribution, only a finite (and relatively small) number of sand grains are included in the calculations. For $\overline{k} = 3 \times 10^{-4}$, the number of sand grains in the domain is approximately 2×10^4, whereas for $\overline{k} = 9.5 \times 10^{-4}$ it is decreased by a factor of 10. To verify that the drag calculation was not affected by insufficient sample, we use the time-averaged f_d in cases K1R1 and K3R1, which are among the cases with the largest number of roughness samples (22311 samples) due to the small roughness scale (R1). We performed plane averages over small portions of the domain itself (and, thus, a smaller number of roughness elements). We then evaluated the root-mean-square of the plane-averaged force, for various subdomains, and compared it with that obtained from the entire domain. Figure 29 shows the root-mean-square (RMS) variation of the force averaged over a subset containing n_r roughness elements. As $n_r \to \infty$, of course, the RMS approaches zero (the sample of roughness elements becomes adequate). For the domain containing 1000-3000 roughness samples, the standard deviation of the force is around 1%-2% of the mean force. Given that more than 2000 samples are used in each case, the sampling is considered sufficient. Note also that the comparison between K1R1 and K3R1 shows that the variation of k^+ within the transitionally rough regime does not affect significantly the f_d uncertainty.

REFERENCES

[1]M. R. Raupach and A. S. Thom, "Turbulence in and above plant canopies," Annu. Rev. Fluid Mech. **13**, 97–129 (1981).

[2]M. R. Raupach, R. A. Antonia, and S. Rajagopalan, "Rough-wall boundary layers," App. Mech Rev. **44**, 1–25 (1991).

[3]J. Finnigan, "Turbulence in plant canopies," Annu. Rev. Fluid Mech. **32**, 519–571 (2000).

[4]J. Jiménez, "Turbulent flows over rough walls," Annu. Rev. Fluid Mech. **36**, 173–196 (2004).
[5]P.-Å. Krogstad, R. A. Antonia, and L. W. B. Browne, "Comparison between rough-and smooth-wall turbulent boundary layers," J. Fluid Mech. **245**, 599–617 (1992).
[6]M. F. Tachie, D. J. Bergstrom, and R. Balachandar, "Roughness effects in low-Re_θ open-channel turbulent boundary layers," Exp. Fluids **35**, 338–346 (2003).
[7]M. P. Schultz and K. A. Flack, "Outer layer similarity in fully rough turbulent boundary layers," Exp. Fluids **38**, 328–340 (2005).
[8]G. J. Kunkel, J. J. Allen, and A. J. Smits, "Further support for Townsend's Reynolds number similarity hypothesis in high Reynolds number rough-wall pipe flow," Phys. Fluids **19**, 055109–1—6 (2007).
[9]P.-Å. Krogstad and R. A. Antonia, "Surface roughness effects in turbulent boundary layers," Exp. Fluids **27**, 450–460 (1999).
[10]R. J. Volino, M. P. Schultz, and K. A. Flack, "Turbulence structure in a boundary layer with two-dimensional roughness," J. Fluid Mech. **635**, 75–101 (2009).
[11]Y. Wu and K. T. Christensen, "Outer-layer similarity in the presence of a practical rough-wall topography," Phys. Fluids **19**, 085108–1—15 (2007).
[12]R. Mejia-Alvarez and K. T. Christensen, "Low-order representations of irregular surface roughness and their impact on a turbulent boundary layer," Phys. Fluids **22**, 015106–1—20 (2010).
[13]K. A. Flack and M. P. Schultz, "Review of hydraulic roughness scales in the fully rough regime," Journal of Fluid Engineering **132**, 041203–1—10 (2010).
[14]P. Orlandi and S. Leonardi, "Direct numerical simulation of three-dimensional turbulent rough channels: parameterization and flow physics," J. Fluid Mech. **606**, 399–415 (2008).
[15]K. Bhaganagar, J. Kim, and G. N. Coleman, "Effect of roughness on wall-bounded turbulence," Flow, Turb. Combust. **72**, 463–492 (2004).
[16]K. Bhaganagar, G. N. Coleman, and J. Kim, "Effect of roughness on pressure fluctuations in a turbulent channel flow," Phys. Fluids **19**, 028103–1—4 (2007).
[17]K. Bhaganagar, "Direct numerical simulation of unsteady flow in channel with rough walls." Phys. Fluids **20**, 101508–1—15 (2008).
[18]A. Scotti, "Direct numerical simulation of turbulent channel flows with boundary roughened with virtual sandpaper," Phys. Fluids **18**, 031701–1—4 (2006).
[19]S.-H. Lee and H. J. Sung, "Direct numerical simulation of the turbulent boundary layer over a rod-roughened wall," J. Fluid Mech. **584**, 125–146 (2007).
[20]J. H. Lee, H. J. Sung, and P.-Å. Krogstad, "Direct numerical simulation of the turbulent boundary layer over a cube-roughened wall," J. Fluid Mech. **669**, 397–431 (2011).
[21]S. Leonardi, P. Orlandi, R. J. Smalley, L. Djenidi, and R. A. Antonia, "Direct numerical simulations of turbulent channel flow with transverse square bars on one wall," J. Fluid Mech. **491**, 229–238 (2003).
[22]T. Ikeda and P. A. Durbin, "Direct simulations of a rough-wall channel flow," J. Fluid Mech. **571**, 235–263 (2007).
[23]R. Narasimha and K. R. Sreenivasan, "Relaminarization of fluid flows," in *Adv. Applied Mech.*, Vol. 19 (Academic Press Professional, Inc., New York, 1979) pp. 221–309.
[24]P. Spalart, "Numerical study of sink-flow boundary layers," J. Fluid Mech. **172**, 307–328 (1986).

[25]R. Narasimha and K. R. Sreenivasan, "Relaminarization in highly accelerated turbulent boundary layers," J. Fluid Mech. **61**, 417–447 (1973).
[26]R. Narasimha, "The laminar-turbulent transition zone in the boundary layer," Prog. Aerosp. Sci. **22**, 29–80 (1985).
[27]C. Bourassa and F. O. Thomas, "An experimental investigation of a highly accelerated turbulent boundary layer," J. Fluid Mech. **634**, 359–404 (2009).
[28]U. Piomelli and J. Yuan, "Numerical simulations of spatially developing, accelerating boundary layers," Phys. Fluids **25**, 101304–1—21 (2013).
[29]U. Piomelli, E. Balaras, and A. Pascarelli, "Turbulent structures in accelerating boundary layers," J. Turbul. **1**, 1–16 (2000).
[30]G. De Prisco, A. Keating, and U. Piomelli, "Large-eddy simulation of accelerating boundary layers," AIAA Paper 2007-0725 (2007).
[31]W. P. Jones and B. E. Launder, "Some properties of sink-flow turbulent boundary layers," J. Fluid Mech. **56**, 337–351 (1972).
[32]M. B. Jones, I. Marusic, and A. E. Perry, "Evolution and structure of sink-flow turbulent boundary layers," J. Fluid Mech. **428**, 1–27 (2001).
[33]D. M. McEligot and H. Eckelmann, "Laterally converging duct flows. Part 3. Mean turbulence structure in the viscous layer," J. Fluid Mech. **549**, 25–59 (2006).
[34]S. A. Dixit and O. N. Ramesh, "Large-scale structures in turbulent and reverse-transitional sink flow boundary layers," J. Fluid Mech. **649**, 233–273 (2010).
[35]M. F. Tachie, M. Agelin-Chaab, and M. K. Shah, "Turbulent flow over transverse ribs in open channel with converging side walls," Int. J. Heat Fluid Flow **28**, 683—707 (2007).
[36]M. F. Tachie and M. Shah, "Favorable pressure gradient turbulent flow over straight and inclined ribs on both channel walls," Phys. Fluids **20**, 095103–1—22 (2008).
[37]R. B. Cal, B. Brzek, T. G. Johansson, and L. Castillo, "Influence of the external conditions on transitionally rough favorable pressure gradient turbulent boundary layers," J. Turbul. **9**, 38–1—22 (2008).
[38]R. Cal, B. Brzek, T. Johansson, and L. Castillo, "The rough favourable pressure gradient turbulent boundary layer," J. Fluid Mech. **641**, 129–155 (2009).
[39]C. Meneveau, T. S. Lund, and W. H. Cabot, "A Lagrangian dynamic subgrid-scale model of turbulence," J. Fluid Mech. **319**, 353–385 (1996).
[40]A. Keating, U. Piomelli, K. Bremhorst, and S. Nešić, "Large-eddy simulation of heat transfer downstream of a backward-facing step," J. Turbul. **5**, 20–1—27 (2004).
[41]R. J. Volino, M. P. Schultz, and K. A. Flack, "Turbulence structure in rough-and smooth-wall boundary layers," J. Fluid Mech. **592**, 263–293 (2007).
[42]Y. Wu and K. T. Christensen, "Spatial structure of a turbulent boundary layer with irregular surface roughness," J. Fluid Mech. **655**, 380–418 (2010).
[43]S. A. Dixit and O. N. Ramesh, "Pressure-gradient-dependent logarithmic laws in sink flow turbulent boundary layers," J. Fluid Mech. **615**, 445–475 (2008).
[44]C. F. Colebrook, "Turbulent flow in pipes with particular reference to the transition region between smooth- and rough-pipe laws," J. Inst. Civ. Eng. **11**, 133–156 (1939).
[45]J. Wallace, H. Eckelmann, and R. Brodkey, "The wall region in turbulent shear flow," J. Fluid Mech. **54**, 39–48 (1973).
[46]J. Kim, P. Moin, and R. D. Moser, "Turbulence statistics in fully developed channel flow at low Reynolds number," J. Fluid Mech. **177**, 133–166 (1987).

[47]A. J. Grass, "Structural features of turbulent flow over smooth and rough boundaries," J. Fluid Mech. **50**, 233–255 (1971).
[48]J. Hong, J. Katz, and M. P. Schultz, "Near-wall turbulence statistics and flow structures over three-dimensional roughness in a turbulent channel flow," J. Fluid Mech. **667**, 1–37 (2011).
[49]S. Talapatra and J. Katz, "Coherent structures in the inner part of a rough-wall channel flow resolved using holographic PIV," J. Fluid Mech. **711**, 161–170 (2012).
[50]R. J. Adrian, C. D. Meinhart, and C. D. Tomkins, "Vortex organization in the outer region of the turbulent boundary layer," J. Fluid Mech. **422**, 1–54 (2000).
[51]P.-Å. Krogstad and R. A. Antonia, "Structure of turbulent boundary layers on smooth and rough walls," J. Fluid Mech. **277**, 1–21 (1994).
[52]S. K. Robinson, "Coherent motions in the turbulent boundary layer," Annu. Rev. Fluid Mech. **23**, 601–639 (1991).
[53]D. Bogard and W. Tiederman, "Burst detection with single-point velocity measurements," J. Fluid Mech. **162**, 389–413 (1986).
[54]F. W. Chambers, H. D. Murphy, and D. M. McEligot, "Laterally converging flow. Part 2. Temporal wall shear stress," J. Fluid Mech. **127**, 403–428 (1983).
[55]R. F. Blackwelder and R. E. Kaplan, "On the wall structure of the turbulent boundary layer," J. Fluid Mech. **76**, 89–112 (1976).
[56]J. Zhou, R. J. Adrian, S. Balachandar, and T. M. Kendall, "Mechanisms for generating coherent packets of hairpin vortices in channel flow," J. Fluid Mech. **387**, 353–396 (1999).
[57]W. Schoppa and F. Hussain, "Coherent structure generation in near-wall turbulence," J. Fluid Mech. **453**, 57–108 (2002).
[58]J. Jiménez and A. Pinelli, "The autonomous cycle of near-wall turbulence," J. Fluid Mech. **389**, 335–359 (1999).